NeuroImage 258 (2022) 119391

Contents lists available at ScienceDirect

NeuroImage

journal homepage: www.elsevier.com/locate/neuroimage

White matter substrates of functional connectivity dynamics in the human brain

Gianpaolo Antonio Basile[a,**], Salvatore Bertino[a], Victor Nozais[b,c], Alessia Bramanti[d], Rosella Ciurleo[e], Giuseppe Pio Anastasi[a], Demetrio Milardi[a], Alberto Cacciola[a,*]

[a] Brain Mapping Lab, Department of Biomedical, Dental Sciences and Morphological and Functional Images, University of Messina, Messina, Italy
[b] Groupe d'Imagerie Neurofonctionnelle, Institut des Maladies Neurodégénératives-UMR 5293, CNRS, CEA, University of Bordeaux, Bordeaux, France
[c] Brain Connectivity and Behaviour Laboratory, Sorbonne Universities, Paris, France
[d] Department of Medicine, Surgery and Dentistry "Medical School of Salerno"- University of Salerno, Italy
[e] IRCCS Centro Neurolesi "Bonino Pulejo", Messina, Italy

ARTICLE INFO

Keywords:
MRI
ICA
Networks
Neuroanatomy
Resting state
Tractography

ABSTRACT

The contribution of structural connectivity to functional connectivity dynamics is still far from being elucidated. Herein, we applied track-weighted dynamic functional connectivity (tw-dFC), a model integrating structural, functional, and dynamic connectivity, on high quality diffusion weighted imaging and resting-state fMRI data from two independent repositories. The tw-dFC maps were analyzed using independent component analysis, aiming at identifying spatially independent white matter components which support dynamic changes in functional connectivity. Each component consisted of a spatial map of white matter bundles that show consistent fluctuations in functional connectivity at their endpoints, and a time course representative of such functional activity. These components show high intra-subject, inter-subject, and inter-cohort reproducibility. We provided also converging evidence that functional information about white matter activity derived by this method can capture biologically meaningful features of brain connectivity organization, as well as predict higher-order cognitive performance.

1. Introduction

Functional co-activation of brain regions, as measured by resting-state functional MRI (rsfMRI), has long been employed to identify spatially segregated patterns of brain activity (Buckner et al., 2009). During the last decades, neuroscience has seen a paradigm shift from a traditional, localizationist view of functional brain organization to a network-based perspective, in which different brain regions, which are frequently engaged together during the execution of complex tasks, tend to show correlated intrinsic activity in awake rest, the so-called resting state (Eickhoff et al., 2011; Smith et al., 2009). Inter-individual differences in activity and configuration of such intrinsic connectivity networks have been shown to reflect differences in perception, cognition and behavior (Raichle, 2015; van den Heuvel et al., 2009).

Recently, this paradigm has been further expanded by incorporating evidence for time-varying fluctuations in functional connectivity strength across brain regions (Preti et al., 2017). This dynamic functional connectivity approach has been employed to parcellate the brain into brain networks akin to those identified by static functional connectivity (Fan et al., 2021), as well as to identify transitions from different states of brain activity in the resting state (Allen et al., 2014), and to predict inter-individual variability in age and cognition (Liu et al., 2018; Qin et al., 2015).

Structural connectivity, resulting either from direct or indirect axonal connections between brain regions, is thought to represent the anatomical substrate of such functional organization. At the current state-of-art, diffusion weighted imaging (DWI) and tractography are instruments of choice for the study of structural connectivity in the human brain in-vivo and non-invasively (Bertino et al., 2021, 2020a; Cacciola et al., 2019, 2016; Milardi et al., 2022). Multimodal approaches integrating tractography with resting-state fMRI have demonstrated a general agreement between structural and func-

* Corresponding author. Alberto Cacciola, MD, Brain Mapping Lab, Department of Biomedical, Dental Sciences and Morphological and Functional Images, University of Messina, Messina, Italy, Phone: +39 0902217143.
** Co-Corresponding author. Gianpaolo Antonio Basile, MD, Brain Mapping Lab, Department of Biomedical, Dental Sciences and Morphological and Functional Images, University of Messina, Messina, Italy, Phone: +39 0902217143.
E-mail addresses: gbasile94@hotmail.it (G.A. Basile), alberto.cacciola0@gmail.com (A. Cacciola).

https://doi.org/10.1016/j.neuroimage.2022.119391.
Received 24 January 2022; Received in revised form 6 June 2022; Accepted 9 June 2022
Available online 15 June 2022.

tional connectivity and between structural and functional brain networks (Honey et al., 2009; Horn et al., 2014; O'Muircheartaigh and Jbabdi, 2018). Notwithstanding, the contribution of structural connectivity to functional connectivity dynamics is still far from being elucidated.

The peculiar spatial organization of functional connectivity is thought to stem in part from the underlying anatomy of white matter circuits, so that some of the system-level properties of functional networks can be explained by the underlying structural connectivity (Honey et al., 2009). At the same time, the intrinsic organization of structural and functional connectivity are expected to diverge, as functional connectivity investigates neuronal activity at a very different time scale compared to synaptic activity and is not constrained by the implicit anatomy of long and short-range neuronal connections. As a clear example of this mismatch, a recent work correlating structural brain networks to functional brain networks found that multiple white matter components accounted for the spatial distribution of each functional brain network (O'Muircheartaigh and Jbabdi, 2018). In this perspective, while most of the existing works analyze functional and structural connectivity data separately, a joint decomposition of both structural and functional information may provide the opportunity of investigating structure-function relationships in a more intuitive fashion (Griffa et al., 2017; Gutiérrez-Gómez et al., 2020).

In addition, evidence suggests that white matter connections have a crucial role in driving and modulating synchronization between brain regions (Finger et al., 2016; Sanchez et al., 2019), which is probably reflected by dynamic fluctuations in brain connectivity (Preti et al., 2017). Hence, incorporating the dynamic connectivity paradigm into this framework provides a simple and natural model to investigate the contribution of structural connectivity in shaping context-dependent fluctuations in functional connectivity in the human brain.

As a member of the track-weighted imaging "family" (Basile et al., 2021; Calamante, 2017; Calamante et al., 2012), track-weighted dynamic functional connectivity (tw-dFC) has been recently developed to allow for a joint analysis of structural and dynamic functional connectivity data (Calamante et al., 2017). By integrating tractography and dynamic functional connectivity information into a unified framework, tw-dFC represents a powerful tool to investigate the relationship between structure and function, as the structural constraints imposed by mapping dynamic functional connectivity on tractography-derived priors provide a solution to the high dimensionality of functional connectivity data.

In the present work, we applied this framework on high spatial and temporal resolution DWI and resting state fMRI (rs-fMRI) data from the Human Connectome Project (HCP) repository (Van Essen et al., 2013). The resulting tw-dFC maps were analyzed using independent component analysis (ICA) at different dimensionality levels, aiming at identifying consistent, spatially independent white matter components which support dynamic changes in functional connectivity. We demonstrated that such components are stable and conserved across different datasets using a test-retest, a split-half approach and data from an independent repository (Leipzig Study for Mind-Body-Emotion Interactions, LEMON) (Babayan et al., 2019). In addition, we provide converging evidence that functional information on white matter activity as derived by this approach can be employed to capture biologically meaningful features of brain connectivity organization, as well as to predict higher-order cognitive performance.

2. Materials and Methods

2.1. Subjects and data acquisition

2.1.1. Primary dataset (HCP)

Structural, diffusion and resting-state functional MRI data of 210 healthy subjects (males=92, females=118, age range 22-36 years) were retrieved from the HCP repository (https://humanconnectome.org). Data have been acquired by the Washington University, University of Minnesota and Oxford University (WU-Minn) HCP consortium. The Washington University in St. Louis Institutional Review Board (IRB) approved subject recruitment procedures, informed consent and sharing of de-identified data.

MRI data were acquired on a custom-made Siemens 3T "Connectome Skyra" (Siemens, Erlangen, Germany), provided with a Siemens SC72 gradient coil and maximum gradient amplitude (Gmax) of 100 mT/m (initially 70 mT/m and 84 mT/m in the pilot phase), to improve acquisitions of diffusion-weighted imaging (DWI).

High resolution T1-weighted MPRAGE images were collected using the following parameters: voxel size = 0.7 mm, TR = 2400 ms, TE = 2.14 ms.

DWI data were acquired using a single-shot 2D spin-echo multiband Echo Planar Imaging (EPI) sequence and equally distributed over 3 shells (b-values 1000, 2000, 3000 mm/s^2), 90 directions per shell, spatial isotropic resolution of 1.25 mm.

For rs-fMRI, a gradient-echo EPI resolution was acquired with the following parameters: voxel size = 2mm isotropic, TR = 720 ms, TE = 33.1 ms, 1200 frames, ~15 min/run. Scans were acquired along two different sessions on different days, with each session consisting of a left-to-right (LR) and a right-to-left (RL) phase encoding acquisition; in the present work, we employ left-to-right and right-to-left acquisitions from a single session only (first session) (Glasser et al., 2013; Smith et al., 2013; Uğurbil et al., 2013; Van Essen et al., 2013).

2.1.2. Validation dataset (LEMON)

We obtained structural, diffusion and rs-fMRI data of 213 healthy subjects (males=138, females=75, age range 20-70 years) from the Leipzig Study for Mind-Body-Emotion Interactions (LEMON) dataset (http://fcon_1000.projects.nitrc.org/indi/retro/MPI_LEMON.html). The study was carried out in accordance with the Declaration of Helsinki and the study protocol was approved by the ethics committee at the medical faculty of the University of Leipzig.

MRI was performed on a 3T scanner (MAGNETOM Verio, Siemens Healthcare GmbH, Erlangen, Germany) equipped with a 32-channel head coil.

High resolution structural MRI scans were acquired using a MP2RAGE sequence and with the following parameters: voxel size =1 m, TR = 5000 ms, TE = 2.92 ms.

Single-shell DWI data were acquired using a multi-band accelerated sequence with spatial isotropic resolution= 1.7 mm, b-value=1000, 60 diffusion-encoding directions.

For rs-fMRI data, a gradient-echo EPI was performed with the following parameters: phase encoding = AP, voxel size=2.3 mm isotropic, TR = 1400 ms, TE = 30 ms, 15.30 min/run (Babayan et al., 2019).

2.2. Data preprocessing

2.2.1. Structural preprocessing

All T1-weighted images were obtained in skull-stripped version (Babayan et al., 2019; Glasser et al., 2013) and were subsequently segmented into cortical and subcortical gray matter (GM), white matter (WM) and cerebrospinal fluid (CSF) using FAST and FIRST FSL's tools (https://fsl.fmrib.ox.ac.uk/fsl/fslwiki/). The segmentation outputs were collapsed into a 5-tissue-type (5TT) image that was required later in the tractography pipeline. T1-weighted volumes were also non-linearly registered to the 1-mm resolution MNI 152 asymmetric template using FLIRT and FNIRT from the FSL toolbox. The quality check of the registered T1 images was performed by visual inspection in specific axial, sagittal and coronal sections.

2.2.2. DWI preprocessing

For the HCP dataset, DWI scans were retrieved in a minimally preprocessed form which includes eddy currents, EPI susceptibility-induced

distortion and motion correction, as well as linear registration of structural and DWI images (Glasser et al., 2013).

In contrast, the LEMON DWI scans were obtained in raw format and underwent preprocessing through the dedicated pipeline included in the MRtrix3 software (https://www.mrtrix.org/). It features denoising using Marchenko-Pastur principal component analysis (MP-PCA), removal of Gibbs ringing artifacts, eddy currents, distortion (by exploiting the available reverse-phase encoding scans) and motion correction using EDDY and TOPUP FSL's tools, as well as bias field correction using the N4 algorithm (Tournier et al., 2019; Tustison et al., 2010).

2.2.3. Resting state fMRI preprocessing

Both HCP and LEMON rs-fMRI data were obtained in preprocessed and denoised form.

HCP data preprocessing included the following steps: field inhomogeneity-related artifact correction, motion correction, registration to standard space (MNI152, 2mm resolution), high pass temporal filtering (> 2000 s full width at half maximum) for removal of slow drifts (Glasser et al., 2013), artifact components identification using ICA-FIX (Salimi-Khorshidi et al., 2014) and regression of artifacts and motion-related parameters (Smith et al., 2013). Minimally preprocessed data were additionally band-pass filtered (0.01-0.09 Hz) and the global WM and CSF signal was regressed out to further improve ICA-based denoising (Plachti et al., 2019).

The LEMON dataset processing pipeline included removal of the first 5 volumes to allow for signal equilibration, motion and distortion correction, artifact detection (rapidart) and denoising using component-based noise correction (aCompCor), mean-centering and variance normalization of the time series as well as spatial normalization to MNI 152, 2mm resolution template (Babayan et al., 2019).

Finally, all rs-fMRI volumes were smoothed through convolution with a Gaussian kernel of 6mm full width at half maximum. All the additional preprocessing described above was carried out in the CONN toolbox (Whitfield-Gabrieli and Nieto-Castanon, 2012).

2.3. Tractography and track-weighted dynamic functional connectivity (tw-dFC)

Whole-brain tractograms were obtained for each subject using the following pipeline: first, diffusion signal modeling was performed on the preprocessed DWI data within the constrained-spherical deconvolution (CSD) framework, which estimates white matter Fiber Orientation Distribution (FOD) function from the diffusion-weighted deconvolution signal using a single fiber response function (RF) as reference (Tournier et al., 2008). Specifically, multi-shell HCP DWI data underwent multi-shell multi-tissue (MSMT) CSD signal modeling, an optimized version of the CSD approach which allows for separate response function calculation in WM, GM and CSF, reducing the presence of spurious FOD in voxels containing GM and/or CSF (Jeurissen et al., 2014). To achieve a similar result on the single-shell LEMON data, the diffusion signal was modeled by using single-shell 3-tissue CSD, a variant of the MSMT model optimized for RF estimation in single-shell datasets. Single-Shell 3-Tissue (SS3T)-CSD signal modeling was performed using MRtrix3Tissue (Dhollander et al., 2016), a fork of MRtrix3 software. After signal modeling, whole-brain tractography was performed using the IFOD2 algorithm with default parameters, and by applying the Anatomically-Constrained Tractography (ACT) framework, which makes use of the 5TT map previously obtained from segmentation to improve the biological plausibility of the resulting streamlines (Smith et al., 2012; Tournier et al., 2010).

For the high b-value, multi-shell HCP data, the spherical-deconvolution informed filtering of tractograms (SIFT) (Smith et al., 2015) algorithm was applied to further improve the fit between the reconstructed streamlines and the underlying DWI data, starting from a generated tractogram of 10 million streamlines and filtering it to a final whole-brain tractogram of 1 million streamlines. Since the SIFT algorithm is best suited for high b-value datasets, it was not applied on the single-shell, low b-value LEMON dataset, where instead a whole brain tractogram of 5 million streamlines was generated (note that the number of streamlines is uninfluential to the tw-dFC contrast generation). Whole-brain tractograms for each subject of both datasets were transformed to the MNI 152 standard space by applying the non-linear transformations obtained from structural images. Since each subject's rs-fMRI volumes were already registered to the MNI 152 template, all the following analyses took place in standard space.

For each subject, whole-brain tractograms derived from tractography and preprocessed rs-fMRI time series were combined to generate a 4-dimensional tw-dFC dataset with the same spatial and temporal resolution of the original fMRI time series. In this framework, each white matter voxel's time series reflects the dynamic changes in functional connectivity occurring at the endpoints of the structural pathways traversing that voxel (Calamante et al., 2017). Specifically, the tw-dFC of a voxel v at time window t is defined as:

$$tw-dFC(v,t) = \frac{1}{N_v}\sum_{i=1}^{N_v} FC_i(t)$$

where N_v is the number of tracts *traversing* that voxel; which is saying, tw-dFC of a voxel v at time window t the averaged functional connectivity across all tracts traversing that voxel at time window t. The final tw-dFC volume is a 4-D volume resulting from tw-dFC of partially overlapping time windows. In particular, for each volume, the contribution from each streamline is calculated based on a finite-width sliding time window, centered at the timepoint corresponding to that volume. In our case, a rectangular sliding window with ~40 s length (55 volumes for the HCP data, TR = 0.72 s; 29 volumes for the LEMON data, TR = 1.4 s) was used, as suggested by previous works (Leonardi and Van De Ville, 2015; Preti et al., 2017). As we employed a rectangular window, the overlap between adjacent time windows is given by (tp-1)/tp where tp is the number of time points in the window, thus resulting in an overlap rate of ~0.98. For HCP data analyses, apart from test-retest analysis, tw-dFC derived from LR and RL phase encoding volumes were temporally concatenated for each subject. It is worth to note that to deal with the low SNR deriving from sampling BOLD signal from the grey-white matter interface, we followed the same rationale as in the reference paper (Calamante et al., 2017). The ACT framework (Smith et al., 2012) was employed to ensure streamline endpoints were located exclusively at the gray matter/white matter interface (see above). To minimize partial volume effects with white matter BOLD signal, spatial smoothing with a relatively large Gaussian kernel (6mm FWHM) was applied and the global WM signal was regressed out.

2.4. Group independent component analysis (ICA)

The obtained tw-dFC volumes were analyzed using a spatial group ICA framework as implemented in the Group ICA of FMRI Toolbox (GIFT) (Calhoun et al., 2001; Erhardt et al., 2011). Group analysis was performed separately for the primary dataset (HCP) and the validation dataset (LEMON). Briefly, the pipeline for group ICA analysis involves a first step, in which a subject-level principal component analysis (PCA) is performed for dimensionality reduction purposes, and a second step in which dimensionality-reduced data are temporally concatenated and undergo a secondary PCA dimensionality reduction along directions of maximal group variability. Finally, the group PCA-reduced matrix is decomposed into a given number of independent components (ICs) using the Infomax algorithm (Bell and Sejnowski, 1995).

For the first data reduction step, 120 subject-specific PCA components were chosen, as in previous works (Erhardt et al., 2011). The second data reduction step and subsequent ICA decomposition were performed at three different dimensionality levels (ICA_{10}, ICA_{20} and ICA_{100}). For each run, the ICA algorithm was repeated 20 times in ICASSO and the n most reliable components were identified as the final group-level components, to ensure stability of estimation. ICASSO

returns a stability (quality) index (Iq) for each estimate-cluster. This provides a rank for the corresponding ICA estimate. In the ideal case of *m* one-dimensional independent components, the estimates are concentrated in *m* compact and close-to-orthogonal clusters. In this case, the index to all estimate-clusters is very close to one, while it drops when the clusters grow wider and less homogeneous (Sai Ma et al., 2011).

Finally, the resulting components for each run were visually inspected to ensure that: 1) the peak activation of each network was localized in the white matter; 2) there was only minimal overlap to vascular, meningeal, ventricular sources of artifacts; 3) the mean power spectra of each network showed prominence of low frequency spectral power.

For each component, subject-specific spatial maps and time courses were obtained using group-information guided ICA (GIG-ICA) back-reconstruction (Du and Fan, 2013). A one sample t-test was run to generate group statistical maps for each component's spatial map, and a hard parcellation of the white matter was obtained by thresholding the obtained t-maps at z=1. To facilitate the interpretation of the results, spatial maps were annotated by calculating percentage overlap with regions of interest from known GM (Rolls et al., 2020) and WM atlases (Hua et al., 2008; Yeh et al., 2018). For low-level (ICA_{10}) white matter parcellation, components were also labeled in analogy with existing gray matter networks as reported in the previous literature.

2.5. Reproducibility and reliability analysis

The reproducibility of results was evaluated at three different levels on the primary dataset: intra-subject reproducibility (test-retest), inter-subject reproducibility (split-half) and inter-cohort reproducibility (comparison with the validation dataset).

For test-retest reproducibility analysis, the LR- and RL-phase encoding acquisitions for each subject were employed as the test and retest data respectively; in the split-half reproducibility analysis, the HCP sample was split in random halves (105 subject each) and the ICA was run separately on each of them; in the external reproducibility analysis, the results from ICA on the primary dataset were directly compared to the results obtained on the validation dataset. In all cases, the comparison metrics were: i) the pairwise Pearson's correlation coefficient between each spatial component and its corresponding component (i.e., the component which scored the highest correlation coefficient); ii) the Dice similarity coefficient (DSC) (Dice, 1945) between the obtained white matter parcellations, i.e. between each component's binarized, z-thresholded group statistical map and the corresponding component map. Finally, we also computed the intra class correlation coefficient (ICC) to assess test-retest (LR vs RL phase encoding acquisition) component reliability. First, for each component we created a specific binary mask derived from group z-thresholded statistical maps, which included voxels belonging to a given component as derived by both LR and RL datasets. Then the corresponding component map from LR and RL respectively has been masked by using the above mentioned specific binary mask. Next, voxel-wise ICCs (Xing and Zuo, 2018; Zuo et al., 2019) between the corresponding components from LR phase encoding acquisition and the corresponding components from RL phase encoding acquisition were calculated to assess the reliability of the component. The result of this process is one 3D ICC map reflecting the component reliability at the voxel level. Based on each ICC map reflecting the reliability of each component, the ICC values were then averaged across voxels. In the present work, voxel-wise ICC computation was performed by using the third ICC defined by (Shrout and Fleiss, 1979) ICC (3,1) according to the following formula:

$$\mathrm{ICC}\ (3,1) = \frac{BMS - EMS}{BMS + (k-1)EMS}$$

In particular, ICC (3,1) estimates the correlation of the subject signal intensities between test-retest data, modeled by a two-way ANOVA, with random subject effects and fixed session effects. In this model, the total sum of squares is split into subject (BMS) and error (EMS) sums of squares; and k is the number of repeated sessions. In this work, ICC (3,1) (single fixed session effects) was chosen because the components were obtained by two different sessions (k=2, LR and RL) which are the only sessions of interest. Reproducibility and reliability analysis was run separately for each ICA dimensionality level (n=10, n=20, n=100).

2.6. Task-based functional network annotation

To provide insights on the functional relevance of the identified white matter components, i.e. to give a measure of how large-scale white matter networks may be involved in the execution of complex tasks, we compared the resting-state spatial maps resulting from the main dataset to the task-based white matter activation maps derived from a recently developed method, namely the Functionnectome (Nozais et al., 2021). Briefly, the Functionnectome projected the BOLD signal from the grey matter onto the white matter. The white matter signal of a voxel was the result of a weighted mean of the BOLD signals from grey matter voxels structurally connected to the said white matter voxel. The weight applied here was the probability of structural connectivity between the grey and white matter voxels. The Functionnectome outputs a 4D volume that was then processed with standard first-level and second level analyses using FSL, thus resulting in task-based z-transformed t-maps reflecting task-based white-matter activation.

To compare these results to the ICs derived from distinct ICA runs, pairwise Pearson's correlation between the z-weighted functionnectome maps and each component's z-map were computed after a thresholding of $z > 0$. We considered correlations significant if the proportion of shared variance between tw-dFC and functionnectome maps was above 5% (e.g., a spatial correlation of $r > 0.22$).

2.7. Connectivity-based component classification

Functional network connectivity (FNC), defined as the pairwise correlation between each pair of IC time courses, was measured on the primary dataset for each ICA dimensionality level. For each run of ICA, we sought to classify components in an unsupervised way based on the similarity of their activity profiles, by performing k-means clustering on the group-average FNC matrix. The optimal number of clusters (k) was determined by plotting the ratio of between-group variance to total variance for increasing values of k and identifying the elbow point (elbow method). To obtain robust cluster centroids, k-means clustering was performed on bootstrap resamples, by iterating clustering 100 times on randomly drawn samples of ~80% of the total subjects (n=168 for the HCP dataset; n=172, for the LEMON dataset); the resulting centroids were then employed to perform clustering on the whole dataset.

2.8. FNC-based cognitive performance prediction tasks

To evaluate the role of tw-dFC-derived FNC in predicting individual cognitive performance, we applied a linear regression model with leave-one-out cross validation (LOOCV) to behavioral measures of cognitive performance available in the HCP database. Behavioral measures of fluid intelligence (Penn Progressive Matrices, HCP_ID: PMAT24_A_CR), cognitive flexibility (Dimensional Change Card Sort, HCP_ID: CardSort_AgeAdj) and sustained attention (Short Penn Continuous Performance Test, HCP_ID: SPCPT_TP) were selected as independent variables. First, behavioral scores were filtered to remove outliers (values > 3 standard deviations distant to the mean) and zeros (subjects in the sample which did not perform the cognitive tests); this step resulted in n=209 subjects being included for the fluid intelligence and cognitive flexibility tasks, and n=207 subjects for the sustained attention task. Then, FNC measures were used as features to predict, independently and separately, each behavioral variable. More specifically, FNC upper triangu-

lar matrices were vectorized to obtain a single feature vector per subject, and underwent a first feature selection step, in which only features with the highest correlation coefficient ($p < 0.01$) to behavioral scores were retained. In particular, a first LOOCV was used to select the features according to the feature occurrence on each LOO step, taking thus the features above the 70 percentile across each LOO iteration. Then, the retained features were then fed into a predictive linear model and predicted scores were generated for each subject using a LOOCV approach, i.e., for each iteration, data from one subject were set aside as test sample and the remaining subjects were used as training set; such step was iterated for all subjects. Finally, the difference between observed and predicted behavioral scores was computed and the residuals were used to obtain a R^2 for each model, as a measure of goodness of fit. The statistical significance of this value was tested using a permutational approach (10,000 permutations), i.e., by iteratively calculating the R^2 after random permutations of the behavioral scores; results were considered significant with $p < 0.01$. The spatial distribution of significant features for each cognitive score has also been assessed.

2.9. "Brain state" vectors identification

The time series of components underwent further clustering analysis aimed at identifying stable or quasi-stable patterns of component activity weights which tend to reoccur over time and across subjects, an analogy to "brain states" described in the dynamic functional connectivity literature (Allen et al., 2014; Fan et al., 2021). For tw-dFC components, we sought to replicate the procedure described in Fan et al., 2021(Fan et al., 2021) for brain state vector identification from dynamic functional connectivity-derived independent components. For simplicity, and in analogy with this work, we employed the subject-specific time series obtained from ICA_{20}. Firstly, we computed subject-specific matrices containing the time course for each component:

$$A_i = \left[a_i^{(1)}, a_i^{(2)}, \ldots a_i^{(t)}\right]^T$$

where i is a subject and a is the activity vector of each component at each timepoint t. To reduce redundancy and temporal autocorrelation between time windows, and decrease the computational load, we downsampled the time points at the rate of 10 (i.e. retaining one time window each ten).

Data for all m subjects were concatenated together $\{a_i^{(1)}, a_i^{(2)}, \ldots a_i^{(T)},\ i = 1, 2, \ldots m\}$ and a distance matrix based on L1 distance function (Manhattan distance) was computed as follows:

$$dist\left(a_i^{t_1}, a_j^{t_2}\right) = \sum_{c=1}^{n} \mid a_{i,c}^{t_1} - a_{j,c}^{t_2} \mid$$

where $a_{i,c}^{t_1}$ refers to the time-varying activity of c_{th} independent component at time window t_1 for subject i and $a_{j,c}^{t_2}$ is defined similarly. The Ward's method of agglomerative hierarchical clustering (Ward, 1963) was applied to the resulting distance matrix. To determine the optimal number of clusters (k), a cluster validity index (CVI) was computed as the ratio of within-cluster to between-clusters distance. To obtain robust cluster centroids, clustering was performed on bootstrap resamples, by iterating the algorithm 100 times on randomly drawn samples composed by ~80% of the total subjects (n=168 for the HCP dataset; n=172, for the LEMON dataset). Consequently, all the time points were classified into k clusters, each including time windows with a similar pattern of component activity. To make the results more easily interpretable and recover information on how each component behaves in these time windows, brain states were visualized as vectors obtained by averaging each component's activity weights at the time points falling within the same cluster. A complete representation of the whole processing pipeline is provided in Fig. 1.

3. Results

For each subject, whole-brain tractograms derived from tractography and preprocessed rs-fMRI time series were combined to generate a 4-dimensional tw-dFC dataset with the same spatial and temporal resolution of the original fMRI time series. In this framework, each white matter voxel's time series reflects the dynamic changes in functional connectivity occurring at the endpoints of the white matter pathways traversing that voxel.

3.1. ICA-based parcellation of tw-dFC reveals white matter networks, sub-networks, and functional units

The obtained tw-dFC volumes were analyzed using a spatial group ICA that resulted in a series of well-recognizable, anatomically meaningful patterns of white matter connectivity. Each component consisted of a white matter spatial map, which represents the spatial distribution of white matter bundles which show consistent fluctuations in functional connectivity at their endpoints, and a time course that is representative of the dynamic connectivity fluctuations occurring along these tracts. ICA decomposition was performed at three different dimensionality levels, by selecting a different number of components (n) for each run: a first run with n=10 (ICA_{10}), to reveal large-scale networks; a second run with n=20 (ICA_{20}) which has been commonly used empirically to identify consistent resting-state networks (Damoiseaux et al., 2006; Fan et al., 2021) and a third run with n=100 (ICA_{100}) to obtain a more fine-grained parcellation. For each of these three group ICA runs, and both for the principal dataset (HCP) and the validation dataset (LEMON), peak activation for each independent component (IC) was localized in the white matter; all the components' mean power spectra show higher low-frequency spectral power and for all the reconstructed components there was no or minimal overlap with known vascular, ventricular, and meningeal sources of artifacts (Supplementary File 1). To ensure stability of estimation, each ICA algorithm was repeated 20 times in ICASSO (Sai Ma et al., 2011). On the principal datasets, the cluster stability/quality index (I_q) over 20 ICASSO runs was very high (> 0.9) for all the components. Similar results were obtained on the validation dataset, except for the n=100 run, where nearly all components obtained moderate-to-high I_q values (>0.8) (Supplementary Figure 1).

For the lower-dimensionality ICA_{10}, the resulting components mostly consisted of white matter pathways linking nodes of well-known gray matter functional networks derived from rs-fMRI literature: default mode network (IC3), lateral (IC5) and medial (IC1) sensorimotor network, right (IC6) and left (IC7) frontoparietal network, lateral (IC9) and medial (IC9) visual network and auditory network (IC4) (Fig. 2).

The ICA_{20} parcellation retrieved a more detailed representation of the networks featured in the lower dimensionality ICA run, and some of the networks were split into distinct sub-networks. In addition, along with cortical connectivity networks, a cerebello-cerebellar connectivity component was also identified (IC5). By contrast, the higher-dimensionality ICA_{100} mostly identifies individual white matter bundles (Fig. 3A). While most components are bilateral and symmetric, especially from the low-dimensionality ICA runs, some of the ICs from ICA_{100} are lateralized, and many of them show roughly symmetrical, contralateral counterparts (Supplementary Figure 2). In addition, the patterns of connectivity revealed by the higher-dimensionality ICA also highlighted "functional units" corresponding to the somatotopic subdivision of the sensorimotor cortex, to parallel cortico-basal ganglia circuits, as well as to segregated, intrinsic cerebellar connectivity patterns (Fig. 3B-C-D). Component spatial maps underwent a group statistical analysis (one sample t-test) and the resulting statistical maps were hard-thresholded at z=1to obtain a white matter parcellation for each ICA run. Percentage overlap between white matter parcellations derived from the ICA_{10}, ICA_{20} and ICA_{100} and known white and gray matter components is reported in Supplementary File 2.

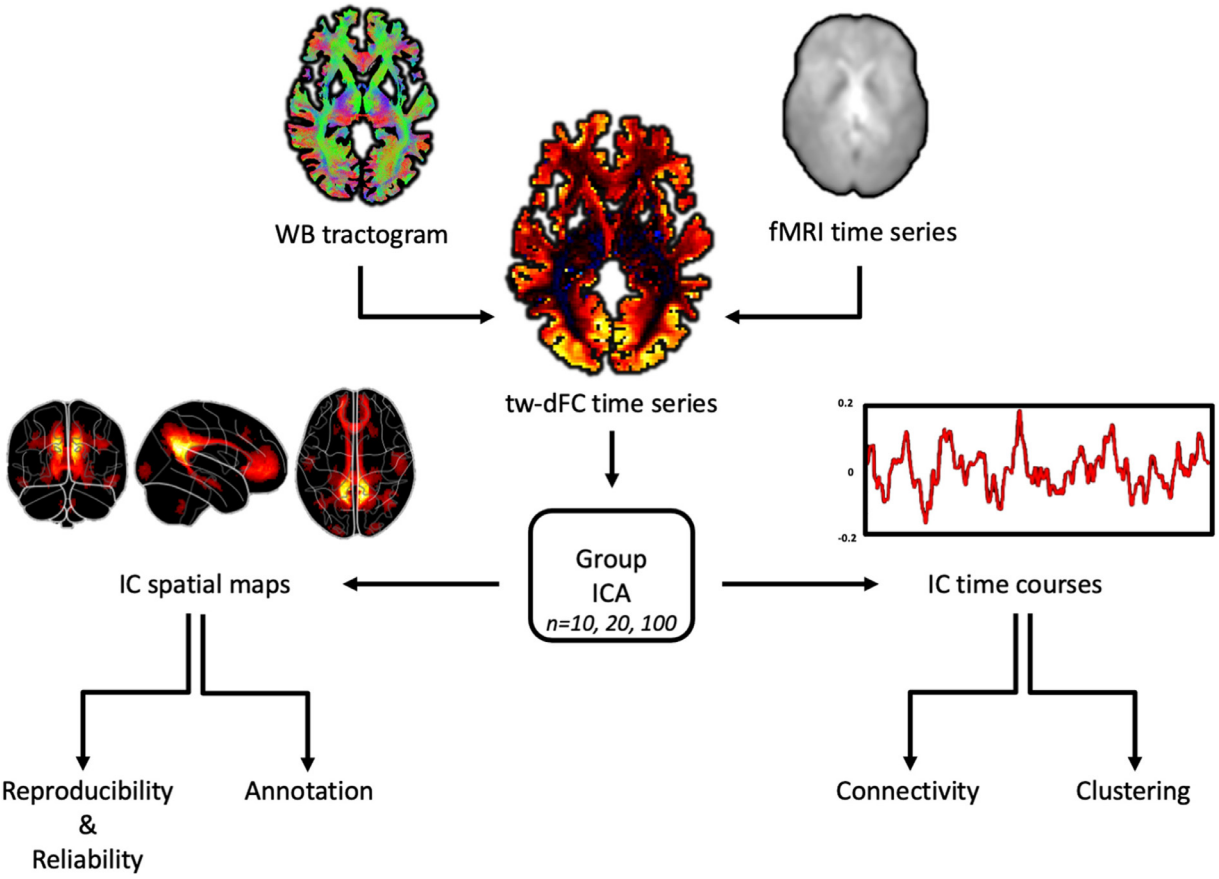

Fig. 1. Overview of the workflow. After diffusion-MRI and fMRI preprocessing steps, whole-brain tractography and resting-state fMRI are merged to generate subject-specific track-weighted dynamic functional connectivity (tw-dFC) time series. Independent component analysis (ICA) is then applied at the group level to classify the tw-dFC signal into spatially independent component (IC) maps and their associated time courses, which are the basis for following analyses. In particular, reproducibility of IC spatial maps was evaluated at three different levels on the primary dataset: intra-subject reproducibility (test-retest), inter-subject reproducibility (split-half) and inter-cohort reproducibility (comparison with the validation dataset). Test-retest components' reliability was assessed by computing the intra class correlation coefficient (ICC). IC spatial maps were also annotated by calculating percentage overlap with regions of interest from known GM (Rolls et al., 2020) and WM atlases (Hua et al., 2008; Yeh et al., 2018). IC time courses, instead, were employed to compute between-components correlation (functional network connectivity, FNC), perform connectivity-based IC classification, and predict cognitive tasks. Finally, the time series of IC underwent a further clustering analysis aimed at identifying stable or quasi-stable patterns of component activity weights which tend to reoccur over time and across subjects, an analogy to "brain states" described in the dynamic functional connectivity literature.

3.2. White matter components show high intra-subject, inter-subject and inter-cohort reproducibility and variable test-retest reliability

The reproducibility of the results was evaluated at three different levels on the primary dataset: intra-subject reproducibility (test-retest), inter-subject reproducibility (split-half) and inter-cohort reproducibility (comparison with the validation dataset).

All the components derived from ICA_{10}, ICA_{20} and ICA_{100} were successfully replicated in the test-retest reproducibility analysis, showing very high or moderate-to-high intra-subject reproducibility. Pearson's correlation was employed to quantify similarity between group spatial maps. Specifically, the ICA_{10} showed the highest test-retest reproducibility (all components with Pearson r = 1, meaning absolute identity between the paired components from the two datasets), while the ICA_{20} and ICA_{100} showed a decreasing trend. Reproducibility was evaluated for the ICA-derived white matter hard parcellations as well, using the DSC as a reproducibility measure. We found a similar trend for the corresponding white matter parcellations: for the ICA_{10} a DSC value > 0.99 was reached for all components, while lower values were obtained by the ICA_{20} and the ICA_{100}. Finally, test-retest reliability was found to be maximal for ICA_{10}, and to decrease with higher dimensionality, being fair for ICA_{20} and low for ICA_{100} (Fig. 4A).

As regards the split-half replicate analysis, slightly lower between-subject reproducibility compared to test-retest reproducibility was found; in particular, the ICA_{10} obtained the highest correlation between corresponding components, followed by the ICA_{20} and the ICA_{100}. For the white matter parcellation, a different trend was observed; while the ICA_{10} obtained the highest DSC values between corresponding components, the ICA_{100} run showed higher spatial overlap than the ICA_{20} (Fig. 4B).

For sake of readability, values of reproducibility and reliability measures are reported in Table 1.

Finally, many of the components resulting from the primary dataset (HCP) were totally or partially replicated in the validation dataset (LEMON) (Fig. 5A). To ease with interpretation of the results, we subdivided correlation values into three ranks: high correlation (r > 0.66), moderate correlation (0.33 < r > 0.66) low or absent correlation (r < 0.33). Fig. 5B shows the components ranked by Pearson's correlation coefficient for each ICA dimensionality. Due to the heterogeneity of the results between the two datasets, DSC between paired components from the two datasets was not calculated. However, corresponding components were visually inspected to check for similar coverage of cortical, subcortical, and white matter regions. Visual inspection confirmed that highly correlated components covered roughly the same cortical, sub-

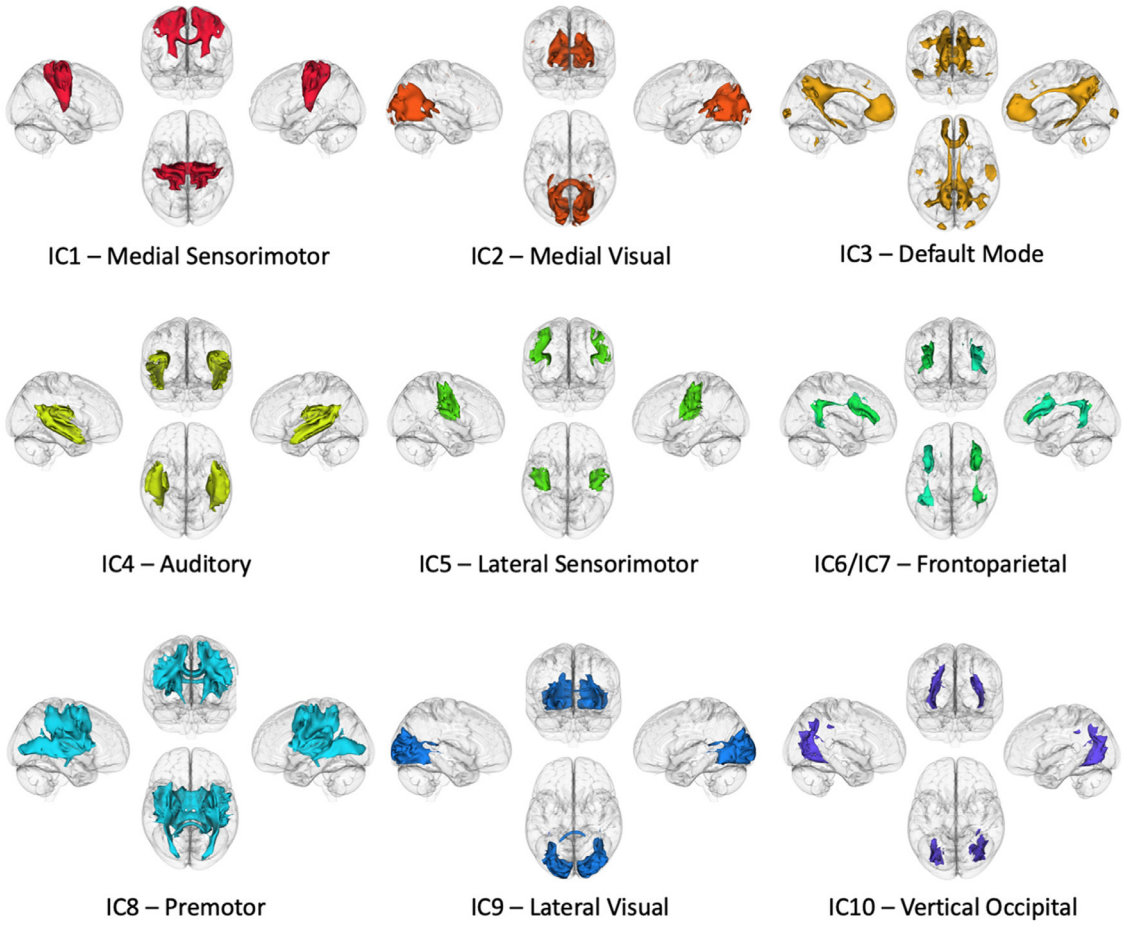

Fig. 2. Large-scale networks as identified by low-dimensionality ICA of tw-dFC data. Independent components (ICs) identified by the ICA_{10} on the main dataset reveal white matter structures corresponding to large-scale brain connectivity networks. Group spatial maps for each component are thresholded at z > 1, binarized and volume-rendered on a glass-brain underlay for visualization purposes. Each render shows left, right, superior, and anterior 3D views, along with the putative large-scale network name attributed to each component.

Table 1
Internal reproducibility and test-retest reliability analysis. The table shows Pearson's correlation values (Pearson's r) and Dice similarity coefficients (DSC) for the test-retest and split-half datasets. The intraclass correlation coefficient (ICC) values computed on the test-retest dataset are also reported. All values are expressed as median (IQR).

	Test-retest			Split-half	
	Pearson's r	*DSC*	*ICC*	*Pearson's r*	*DSC*
ICA_{10}	1 (1-1)	1 (1-1)	1 (1-1)	0.97 (0.99-0.96)	0.88 (0.90-0.85)
ICA_{20}	0.97 (0.98-0.83)	0.78 (0.83-0.55)	0.40 (0.48-0.35)	0.95 (0.98-0.85)	0.71 (0.85-0.59)
ICA_{100}	0.95 (0.97-0.91)	0.64 (0.67-0.58)	0.18 (0.20-0.12)	0.92 (0.95-0.87)	0.81 (0.86-0.75)

cortical, and white matter regions (i.e., they have substantially the same anatomical meaning). Components showing moderate correlation were anatomically distinct, but shared some degrees of overlap, while components with low or absent correlation were completely distinct (Fig. 5C).

3.3. Resting-state and task-based white matter networks are correlated together

Given that resting-state patterns of brain activity are often related to regional coactivation during behavioral tasks (Smith et al., 2009), we sought to investigate the involvement of resting-state white matter dynamic connectivity components in task-modulated activity by correlating them with distinct, task-dependent white matter networks obtained from track-weighted, task-based fMRI data ("Functionnectome"). In brief, the Functionnectome algorithm maps the function signal from fMRI to tractography-derived priors of white matter anatomy. It has been applied to task-based fMRI data from the HCP dataset to obtain group task-based activation maps for the HCP motor, working memory and semantic language tasks (Nozais et al., 2021). As expected, we found high correlation between resting-state and task-based white matter networks. As an example, for the lowest dimensionality ICA run (ICA_{10}), components covering sensorimotor regions (IC1, IC5 and IC8) showed relatively high correlation (r > 0.30) with the motor task-based functionnectome maps (corresponding to left and right finger tapping and left and right toe clenching). The medial, lateral and vertical occipital visual network components (IC2, IC9, IC10) and default mode network component (IC3) were not strongly correlated to any of the task-based functionnectome maps. The auditory network component IC4 was

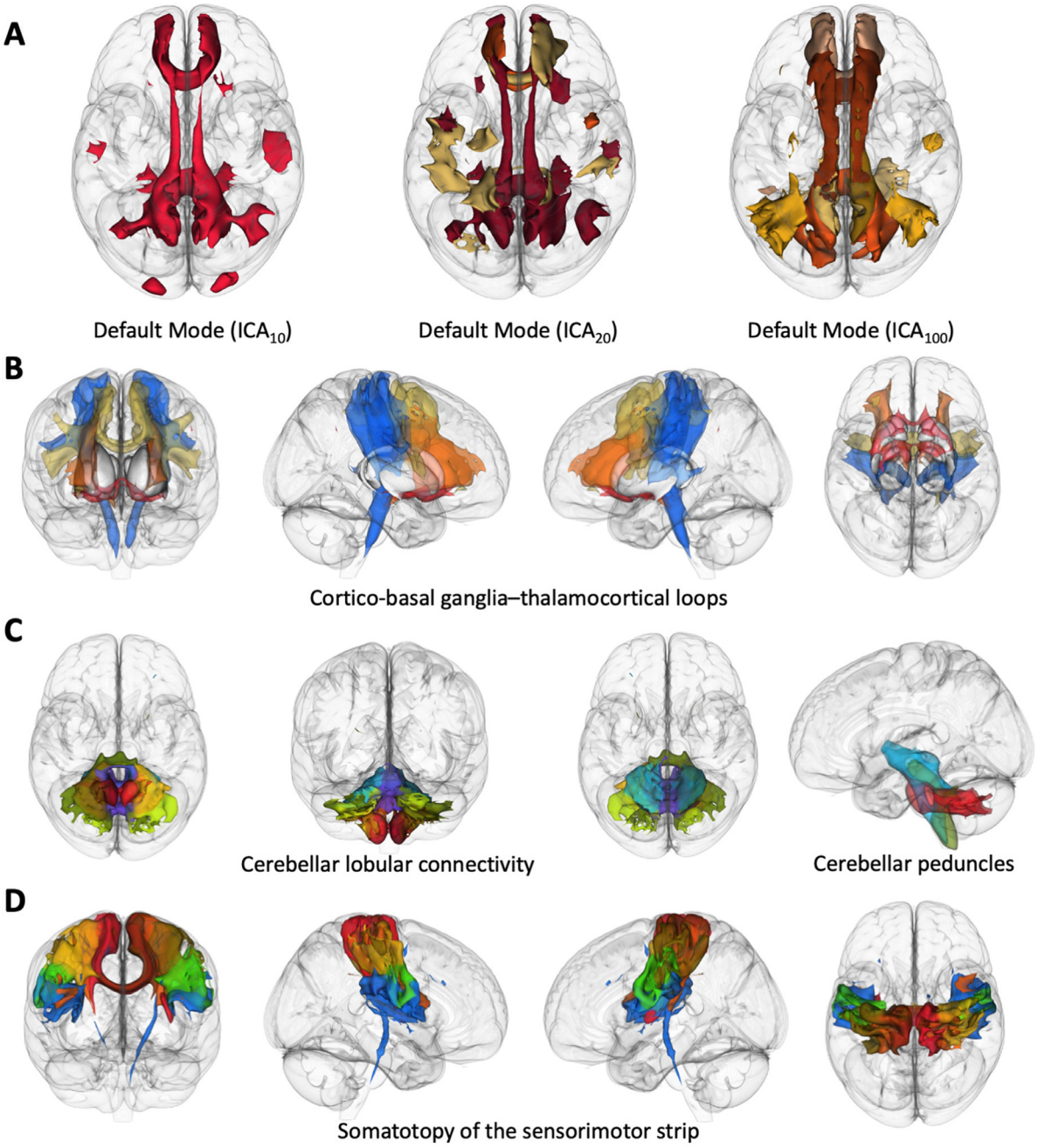

Fig. 3. Anatomical details of white matter organization. Group spatial maps for each component are thresholded at z > 1, binarized and volume-rendered on a glass-brain for visualization purposes. A) Increasing ICA dimensionality splits large scale white matter networks (e.g. the default mode network white matter component, IC3, n=10) into smaller sub-networks (left anterior, IC1; right anterior; IC18; posterior, IC20, n=20) and increasingly detailed white matter sub-units (ICs 12, 30, 49, 50, 56, 68, 81, n=100). B) Cortico-basal ganglia-thalamocortical loops as revealed by ICA_{100} (ICs 72, 84, 38, 42, 87). Fine-grained ICA unsupervised decomposition identifies a ventromedial-orbitofrontal component (red) which extends to the basal forebrain, a ventrolateral component (orange) and dorsolateral (yellow) component involving prefrontal white matter, and two lateralized sensorimotor components (light blue) which also include part of the pyramidal tract. C) Intra-cerebellar connectivity networks (ICs 21, 29, 39, 80, 2, 40, 19, 24, 1, 14, 15, 16, 37) are mostly lobule-specific and include distinct cerebellar white matter regions (likely corresponding to cortico-deep nuclear connectivity); superior, middle and inferior cerebellar peduncles are roughly circumscribed by specific components. D) Components spanning between the sensorimotor strip (precentral and postcentral gyrus) (ICs 5, 11, 13, 31, 33, 35, 44, 75) roughly reflect the somatotopic organization of primary motor and primary somatosensory cortex.

weakly correlated to the language semantic task-based functionnectome map (r = 0.24). Left and right frontoparietal components (IC6 and IC7) showed higher correlation to the working memory task-based functionnectome map (r = 0.40 both). Generally lower correlation to task-based maps were found for ICA_{20} or ICA_{100}, in line with the finding that increasing ICA dimensionality leads to spatially circumscribed components, in contrast with the widespread task-activation maps. However, some components still showed high correlation to task-based maps, suggesting their possible involvement in language, working memory or motor tasks (Fig. 6).

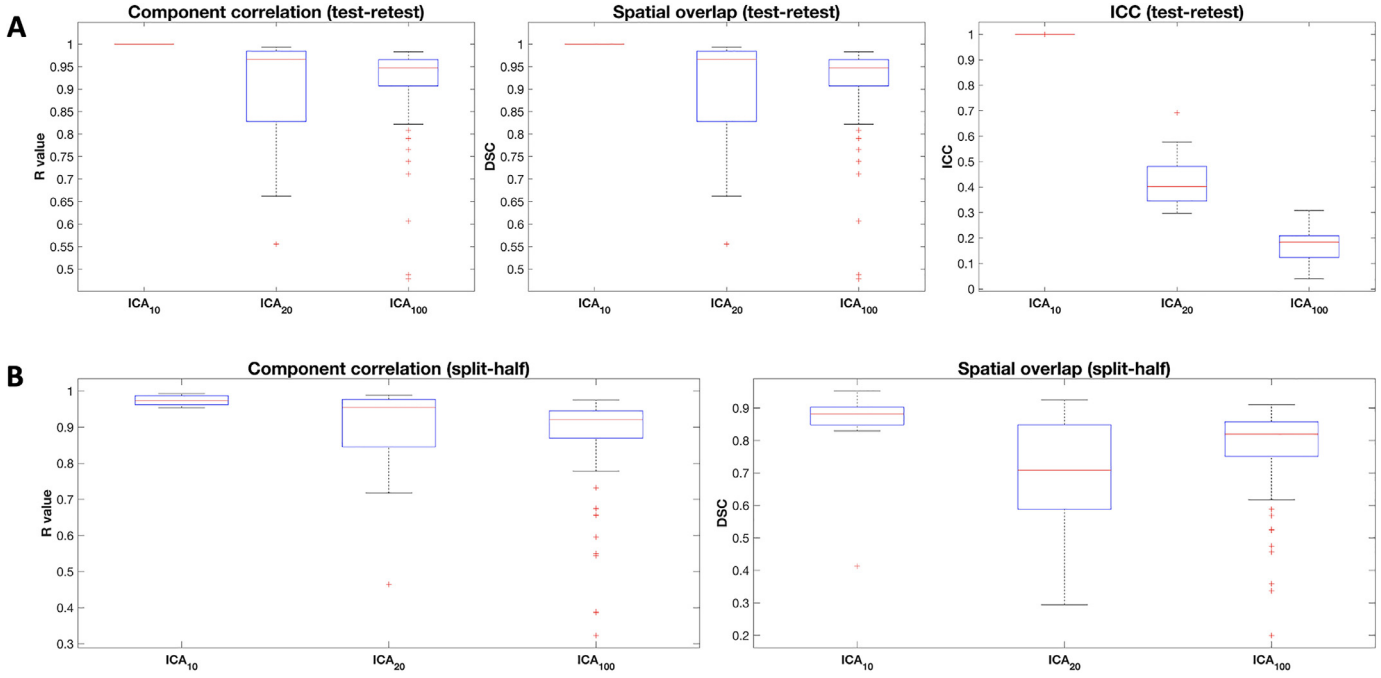

Fig. 4. Internal reproducibility and reliability analysis. A) Box plots showing Pearson's correlation values (left), Dice similarity coefficients (middle) and intraclass correlation coefficient (ICC) (right) between corresponding components from the test-retest dataset. B) Box plots showing Pearson's correlation values (left) and Dice similarity coefficients (right) for the split-half dataset.

3.4. Connectivity-based clustering of independent components uncovers their intrinsic functional organization

Within each different dimensionality ICA run, temporal activity of the extracted ICs, which is a measure of component-specific fluctuations in functional connectivity, showed correlation to that of the other components. Pairwise correlations between components of each run were quantified to obtain ICA-specific "functional network connectivity" (FNC) matrices. Note that the interpretation of connectivity values slightly differ from the classical functional network connectivity as obtained in previous works (Allen et al., 2014). Since tw-dFC volumes are already derived from windowed, dynamic functional connectivity, the time series of tw-dFC derived components are a measure of mean functional connectivity fluctuations at the endpoints of the white matter tracts involved in the IC (i.e., *within* each component). Consequently, FNC can be interpreted as a measure of "co-fluctuation" of the mean functional connectivity *between* pairs of components. As expected, functionally correlated components showed anatomical and functional commonalities that were captured by the clustering analysis of FNC. On the main dataset, the elbow method suggested an optimal number of clusters of k=3 for the ICA_{10}; the following k-means clustering revealed an intrinsic functional organization of ICs into an associative cluster including the default mode, left and right frontoparietal networks, a sensorimotor cluster covering somatomotor, somatosensory, auditory and premotor regions and a visual cluster which includes lateral and medial visual networks as well as a component covering the vertical occipital fasciculus (Fig. 7). Clustering analysis from the ICA_{20} (k=5) and ICA_{100} (k=24) highlighted a roughly similar functional organization into associative, sensorimotor and visual clusters (Supplementary File 2; Supplementary Figures 3-5). In particular, clustering obtained from the higher-dimensionality ICA run showed multiple associative, sensorimotor, visual and cerebellar "sub-clusters", each with distinctive anatomical features, that are likely to represent fine-grained levels of organization of white matter functional activity. FNC clustering based on the validation dataset showed a similar overall organization of clusters (Supplementary Figures 6-9); at ICA_{20} (k=6) and ICA_{100} (k=13), the partitioning into associative, sensorimotor, visual and cerebellar clusters was particularly evident.

3.5. Co-fluctuations of functional connectivity between tw-dFC components predict individual cognitive performance

In order to quantify the role of correlated activity between brain functional units in predicting cognitive performance, we built predictive models based on linear regression using features extracted from individual FNC matrices. In more detail, each feature is constituted by the connectivity strength (Pearson's correlation coefficient) between a pair of ICs from the high dimensional ICA_{100}. LOOCV feature selection (based on correlation between individual connectivity and each behavioral score) resulted in 27 features being correlated to fluid intelligence scores ($p < 0.01$), 34 features being correlated to cognitive flexibility ($p < 0.01$) and 43 features being correlated to sustained attention ($p < 0.01$). The following LOOCV-regression model revealed that each behavioral measure could be effectively predicted by the FNC-derived features (Fig. 8). In particular, the best prediction resulted for fluid intelligence scores ($R^2 = 0.40$, $p < 0.001$), where almost 40% of the inter-individual variance in the behavioral scale was explained by the cross-validated regression model. Cognitive flexibility and sustained attention scores were also successfully predicted by FNC-derived features (cognitive flexibility: $R^2 = 0.35$, $p < 0.001$; sustained attention: $R^2 = 0.37$, $p < 0.001$). FNC-derived features predictive of fluid intelligence mostly involved correlated fluctuations in connectivity between white matter involving the primary sensorimotor cortices, as well as frontoparietal and prefrontal bundles and the right cingulum. Cognitive flexibility was predicted by correlated fluctuations in activity in the white matter connecting frontoparietal, prefrontal and visual regions, as well as the brainstem and cerebellum; finally, sustained attention-related features mostly involved co-fluctuations between intrinsic cerebellar hemispheric connectivity, sensorimotor, prefrontal, frontoparietal and visual cortices.

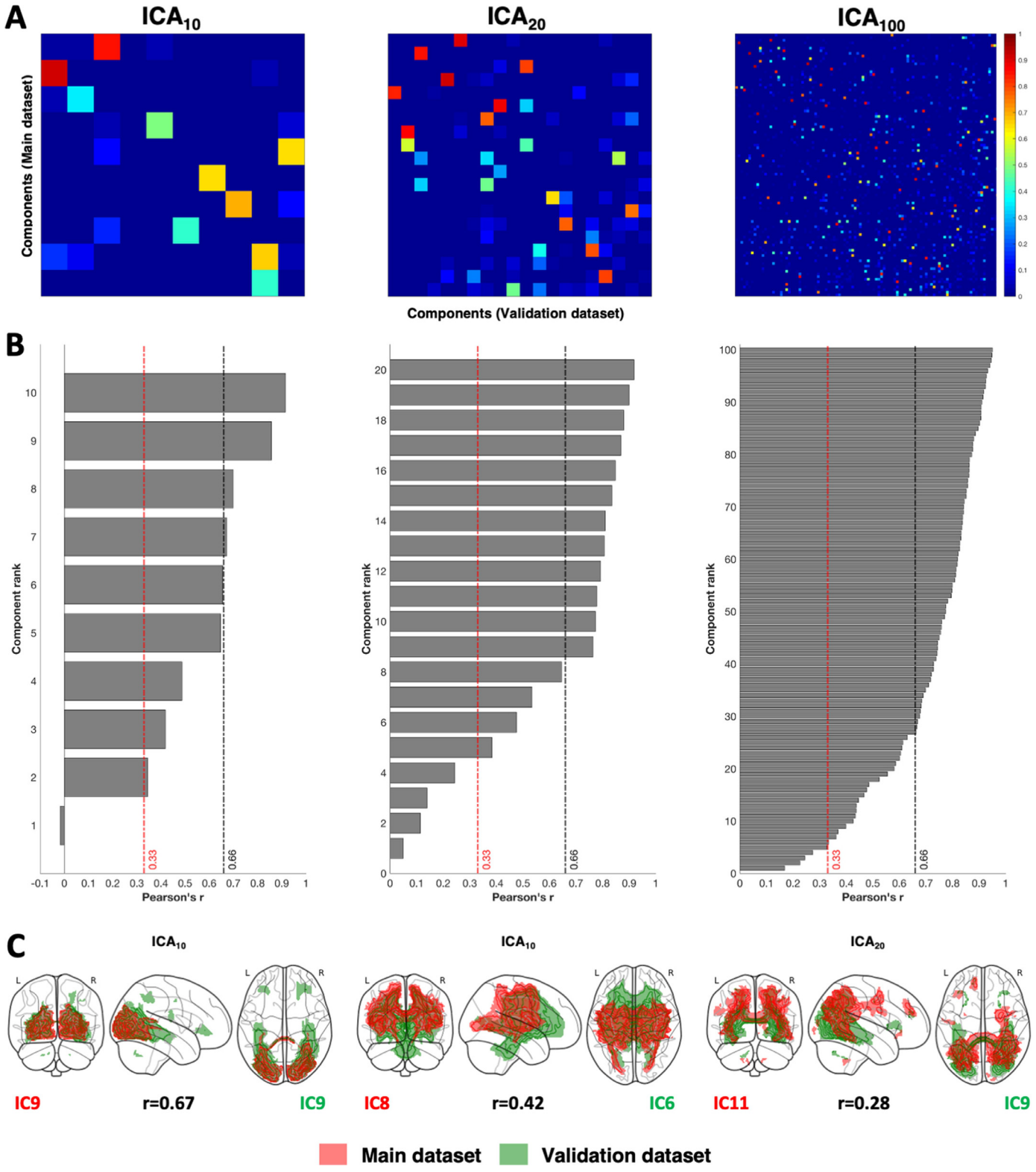

Fig. 5. External reproducibility analysis. A) Matrix plots of the pairwise Pearson's correlation coefficient between the main (HCP) and the validation dataset (LEMON). The colormap allows distinguishing between pairs of components with high correlation (red/yellow), intermediate correlation (green/turquoise) and low correlation (blue/light blue). B) Barplots of the components ranked by Pearson's correlation coefficient between the main and validation datasets. Dashed black and red lines indicate respectively the cut-off for high correlation (r>0.66) and low or absent correlation (r<0.33) respectively. C) A visual example of overlaps between spatial maps of the two independent datasets at different levels of correlation (high, left; moderate, center; low, right). Group spatial maps are thresholded at z > 1, binarized and shown in form of 2D maximum intensity projections on a glass brain in axial, sagittal and coronal sections; L=left; R=right.

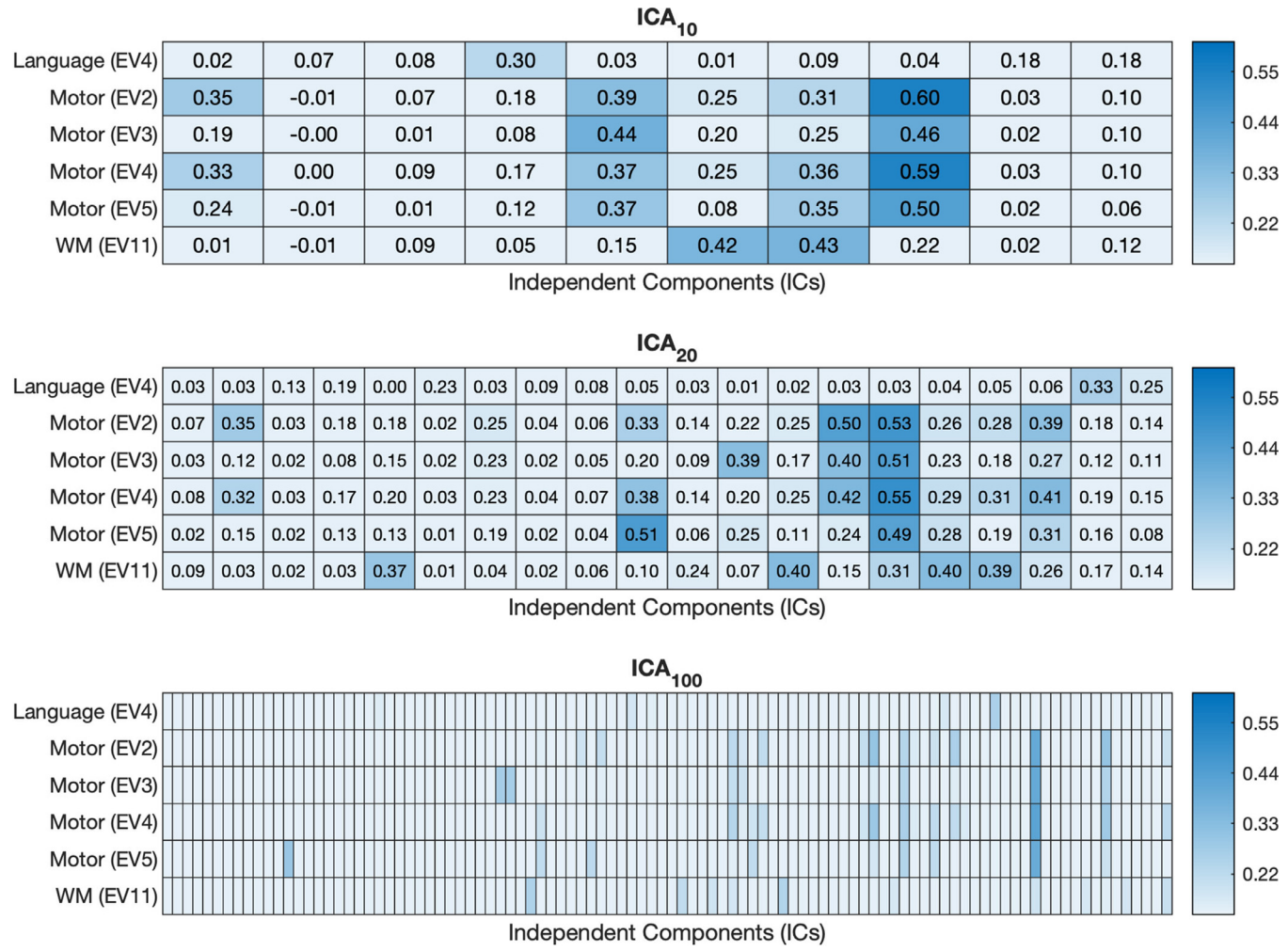

Fig. 6. Correlation between resting-state track-weighted dynamic functional connectivity components (tw-dFC) and task-based white matter activation maps (Functionnectome). The lower threshold was set to 0.22 (i.e., spatial maps which share 5% or above of their variance were deemed to be significantly correlated). Explanatory variables (EV) follow the same nomenclature of the HCP release.

Prediction analysis based on FNC measures from ICA_{10} and ICA_{20} resulted in a few or no features surviving the features selection step and failed at providing statistically significant predictions and acceptable R^2 values.

3.6. Hierarchical clustering of tw-dFC time windows identifies transient "brain states"

Dynamic connectivity shows temporally organized patterns of activity between pairs of nodes or connectivity units, often described as transient "brain states" (Allen et al., 2014; Fan et al., 2021). By applying a hierarchical clustering algorithm to tw-dFC time series, we investigated whether a similar information could be obtained from track-weighted connectivity data. In the main dataset, for hierarchical clustering of tw-dFC time windows an optimal cluster number of k=11 was identified according to the elbow method of CVI, thus resulting in 11 recurring temporal patterns of component activity ("brain states") (Fig. 9). Note that, due to the dynamic and windowed nature of the tw-dFC signal, the term "activity" in this case refers to high or low functional connectivity *within* components, while the FNC previously analyzed referred to correlated variations of functional connectivity *between* components. Brain states analysis for the validation dataset is reported in Supplementary Figure 10. While being not completely identical, brain states identified on the validation dataset are likely to follow roughly the same organizational principles as the main dataset.

4. Discussion

In the present work we employed tw-dFC to incorporate structural and dynamic functional connectivity information into a unified analysis framework (Calamante et al., 2017). In such a framework, the components identified by the ICA process can be interpreted as spatially independent functional units of white matter, composed by fiber bundles sharing coordinated fluctuations of functional connectivity at their endpoints.

On a coarse ICA dimensionality scale, our findings complement and expand current knowledge on resting-state brain networks, as tw-dFC-derived components could be associated with well-known grey matter resting-state networks. Indeed, these ICs mostly consisted of white matter pathways linking nodes of gray matter functional networks as described in rs-fMRI literature during the last decades (Buckner et al., 2009; Fan et al., 2021; Smith et al., 2009). Our results clarify the contribution of anatomical white matter structures to known resting state networks, such as distinct anatomical portions of the corpus callosum in the default mode, medial sensorimotor, medial visual and lateral visual networks (Friedrich et al., 2020), the cingulum bundle in the default mode network (Alves et al., 2019), and the arcuate fasciculi in the left

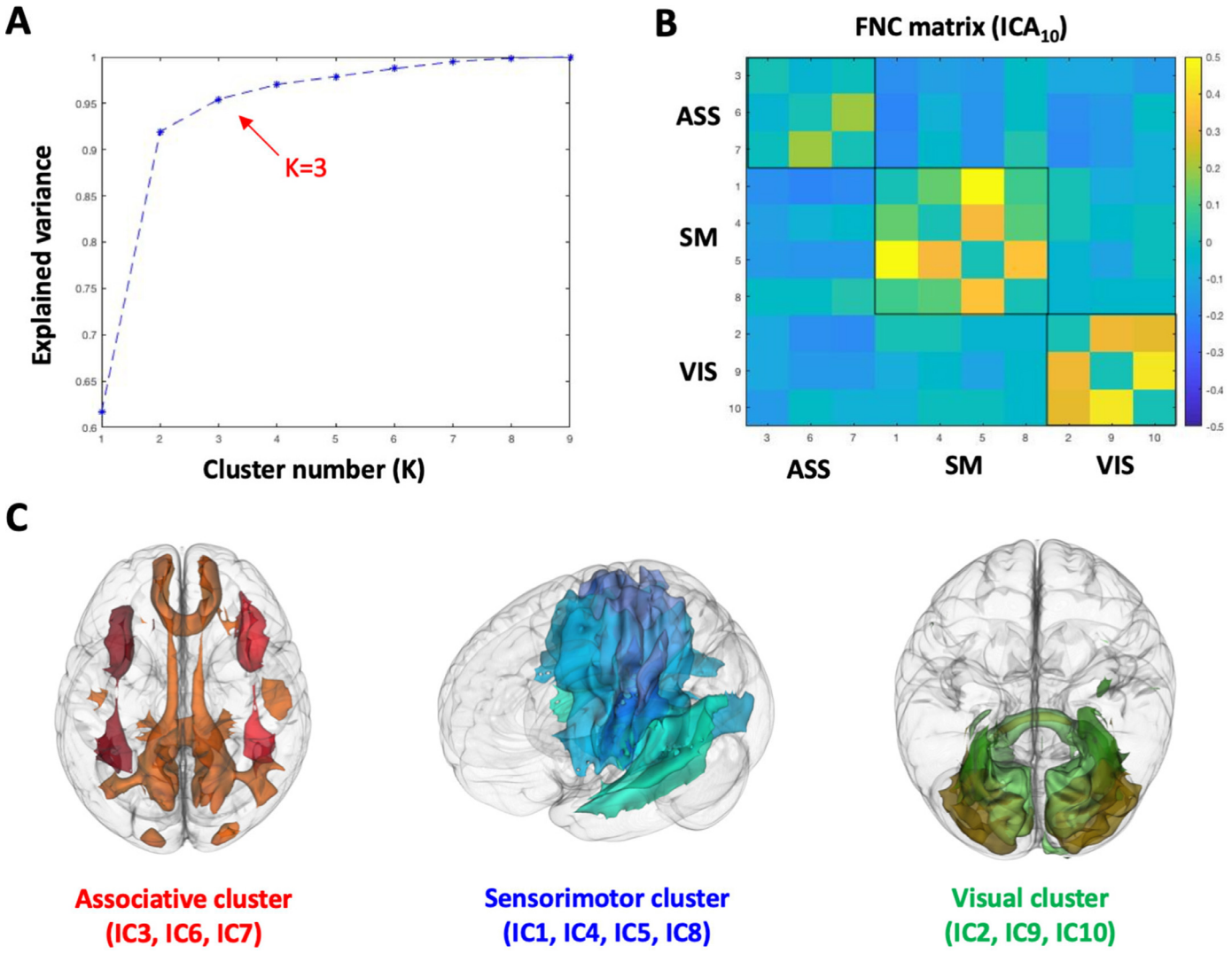

Fig. 7. Functional network connectivity (FNC) clustering analysis (ICA_{10}). A) Plot of the explained variance for different numbers of clusters; the elbow method (red arrow) suggests an optimal number of k=3. B) The FNC matrix, ordered according to the clustering results. Black squares delimitate the three distinct connectivity clusters; ASS = associative, SM = sensorimotor, VIS = visual. C) Visualization of the three FNC-derived clusters; group spatial maps for each component are thresholded at z > 1, binarized and volume-rendered on a glass-brain underlay.

and right frontoparietal networks (Barbeau et al., 2020). While many other works combined tractography and rs-fMRI to identify the white matter correlates of intrinsic brain connectivity networks (Figley et al., 2017), directly decomposing the tw-dFC signal offers the advantage of identifying joint structural/functional connectivity networks in an unsupervised way. In addition, and in line with the existing literature, we confirmed that there is no one-by-one correspondence between white matter bundles and functional brain networks (O'Muircheartaigh and Jbabdi, 2018), as each tw-dFC large scale component included multiple association, commissural and U-fiber tracts.

As expected from previous works (Fan et al., 2021; O'Muircheartaigh and Jbabdi, 2018; Wu et al., 2015), increasing ICA dimensionality has led to a more detailed classification of white matter sub-units. At the most detailed dimensionality scale (ICA_{100}), ICA decomposition of tw-dFC data reveals a fine-grained, anatomically meaningful functional parcellation of the white matter into long- or short-range connectivity patterns, adding further insights on the functional organization of white matter circuits at the macroscale. As an example, fine-grained ICA was able to reveal subtle anatomical details of white matter connectivity such as the dense, tightly-organized U-fibers system connecting somatotopically analogous regions of precentral and postcentral gyri, the contribution of the cerebellar white matter to intrinsic lobule-specific cerebellar circuitry (Guell et al., 2018; Stoodley and Schmahmann, 2018), or again, parallel white matter components corresponding to topographically organized cortico-basal ganglia-thalamic circuitry (Basile et al., 2020; Bertino et al., 2020b; Draganski et al., 2008; Milardi et al., 2019) (Fig. 3).

Similarly to well-known gray matter resting-state intrinsic connectivity networks (Smith et al., 2009), white matter dynamic connectivity networks show correspondence to task-based activation networks. To identify task-based activation networks in the white matter, we employed the results obtained using a recently developed method, the "Functionnectome" (Nozais et al., 2021). Despite substantial differences, this method shows remarkable analogies to the tw-dFC pipeline as they both involve the resampling of functional information derived from BOLD fMRI on anatomical priors derived by tractography, and the representation of outputs in terms of spatial statistical maps (z-maps), thus enabling direct comparison of results. Taken together, the high correlation values obtained between task-based and resting-state dynamic connectivity provide complementary evidence to the hypothesis that regions

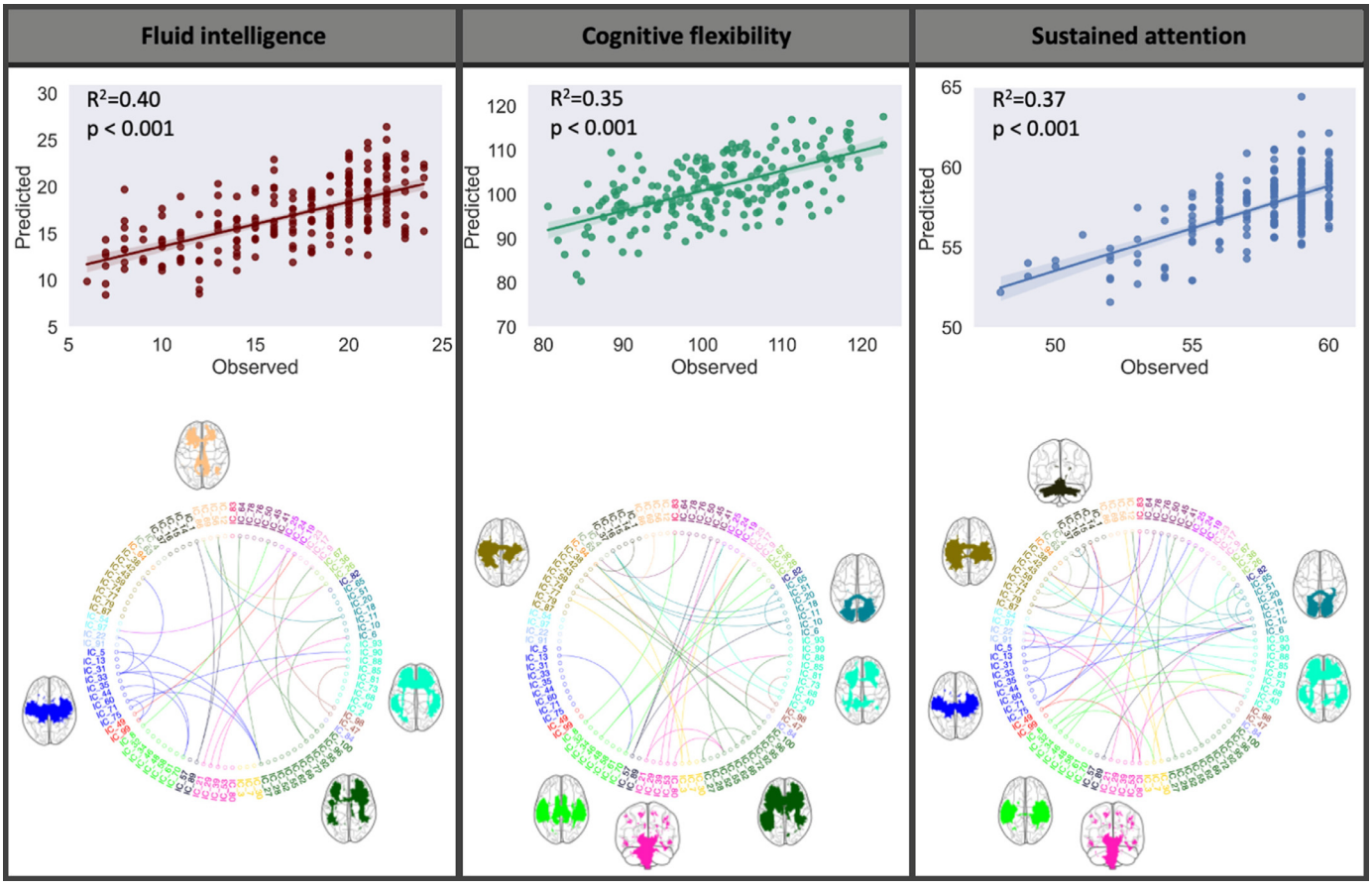

Fig. 8. FNC-based cognitive performance prediction. The upper row shows the observed vs predicted plots for cognitive performance scores of fluid intelligence (Penn Progressive Matrices, age adjusted), cognitive flexibility (Dimensional Change Card Sort), and sustained attention (Short Penn Continuous Performance Test). Each subject's score is represented by a dot and the shaded area around the least square lines is the 95% confidence interval. The bottom row shows the spatial distribution of FNCs predicting fluid intelligence, cognitive flexibility and sustained attention scores respectively. LOOCV prediction analysis identified 27 edges for fluid intelligence, 34 edges for cognitive flexibility and 43 edges for sustained attention. For visualization purpose and to ease spatial interpretation, the glass brains show clusters of components above the 70th percentile of cluster occurrence. Components are colored and grouped into 24 clusters as revealed by FNC clustering analysis (see Results 3.4 and Supplementary Figures 3-5).

intrinsically connected in the resting state are more easily recruited together during tasks (Di et al., 2013; Smith et al., 2009; Tavor et al., 2016).

In addition, spatial tw-dFC components are highly stable both across subjects of the same sample and when compared to those obtained from a validation dataset (Fig. 4). This last result is of utmost importance, as reproducibility is one of the key issues of modern-days neuroimaging research (Nichols et al., 2017). Noteworthy, the validation dataset showed several demographical (larger age range, different gender proportion) and technical differences both in DWI (single shell, low b-value, no filtering) and rs-fMRI (lower temporal resolution, different denoising pipeline). Although a proper formal evaluation of the effects of these variables on the results is warranted in future studies, this finding suggests that tw-dFC-based components may be robust to experimental conditions, and, by consequence, able to capture actual features of brain activity and connectivity regardless of technical differences in data processing. While test-retest and split-half reproducibility showed a progressively decreasing trend with the increase of ICA dimensionality, external reproducibility measures seemed to benefit from high dimensionality; this observation would suggest that, while coarse-scale decomposition may be more influenced by group-specific features of the tw-dFC signal, fine-grained ICA would be in turn less affected by technical and demographic group differences. By contrast, test-retest reliability was found to be maximal for low-level dimensionality and to decrease with higher dimensionality, resulting in excellent ICC values for ICA_{10} and in poor reliability for ICA_{100}. Since reliability has been defined as a statistic on characterizing stochastic processes of individual variability (Xing and Zuo, 2018), this result may suggest that high-dimensionality ICA is less suitable to identify meaningful inter-individual differences.

Aside from providing an unsupervised and reliable functional parcellation of the human white matter, ICA of tw-dFC data has also the advantage of assigning to each white matter component a time course, which allows for direct investigation of time-varying activity of white matter pathways – a difficult task for state-of-art, conventional neuroimaging (Calamante et al., 2017; Nozais et al., 2021). Although a growing body of works employed direct white matter BOLD signal analysis to accomplish such task (Gawryluk et al., 2014; Huang et al., 2020; Peer et al., 2017), sampling BOLD signal from white matter is challenging due to the much smaller number of blood vessels compared to the gray matter, which implies lower signal-to-noise ratio and lower correlations between seed regions (Gawryluk et al., 2014). In addition, the biological mechanisms behind BOLD signal fluctuations in the white matter are still unclear (Smith et al., 2002). In comparison to existing functional networks obtained by clustering of white matter signal (Huang et al., 2020; Peer et al., 2017), the components detected by ICA of tw-dFC show some topographical similarities both at coarse and fine-grained scale, but they are more adherent to the known anatomy of white matter bundles, as a consequence of incorporating white matter priors from multi-fiber tractography into the processing pipeline. This also allows the tw-dFC signal to account for complex fiber configurations such as

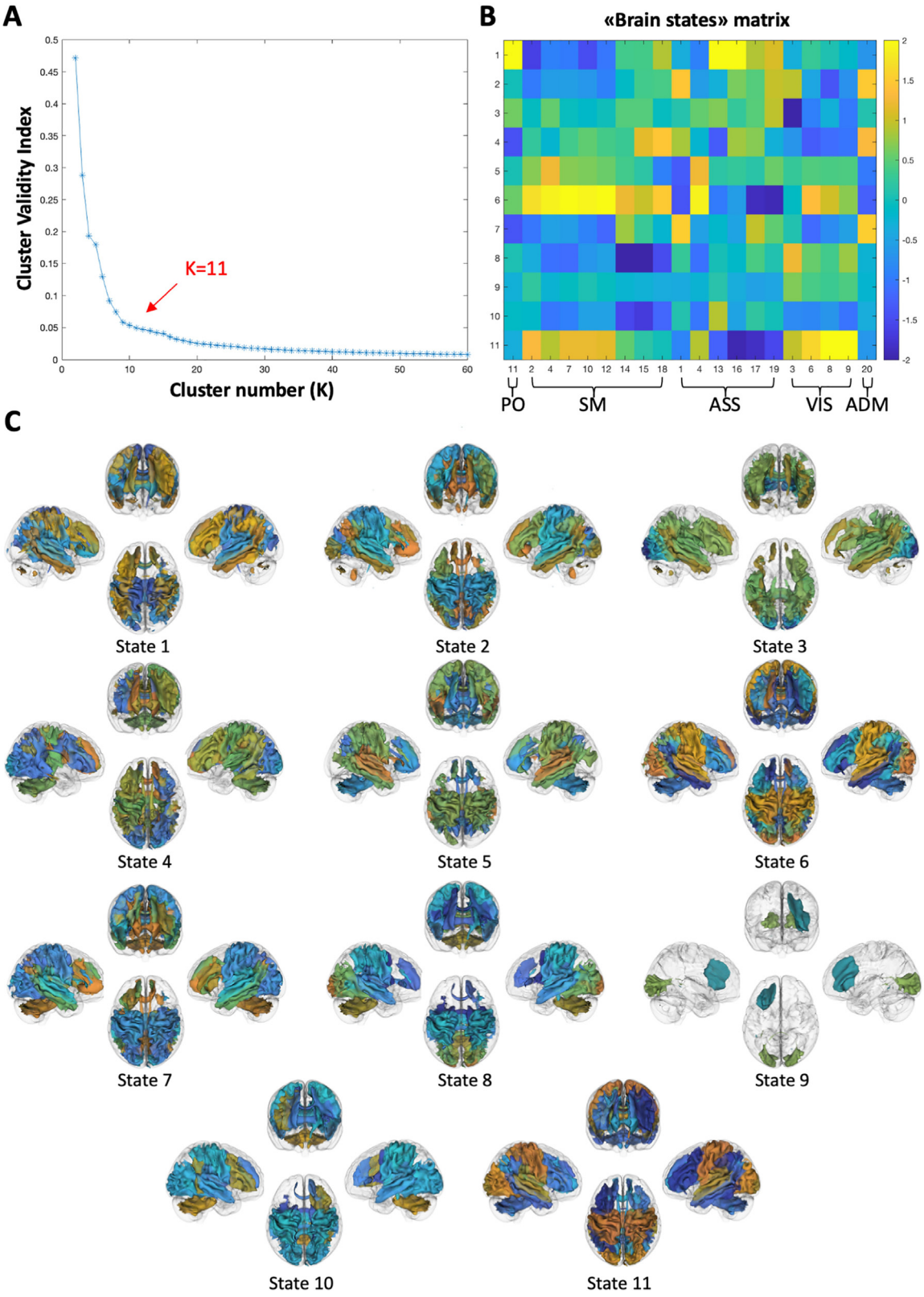

Fig. 9. "Brain states" hierarchical clustering (main dataset). A) The elbow criterion of cluster validity index suggests an optimal cluster number k=11 for hierarchical clustering of tw-dFC time windows. B) Cluster centroids of transient brain state vectors. Colors are assigned according to the average within-component connectivity value in the time windows corresponding to each state, and for each of the n=20 components. Components are sorted according to FNC-based clustering (see Results 3.4 and Supplementary Figures 3-5): PO = parieto-occipital, ASS = associative, SM = sensorimotor, VIS = visual, ADM = anterior default mode. C) Clusters visualization. For each state, group spatial maps of independent components are thresholded at $z > 1$, binarized and volume-rendered on a glass-brain in left, right, anterior, and superior 3D views. For simplicity, only components with average within-component connectivity $r > \pm 0.5$ are displayed. Colormap is the same as in panel B.

crossing, kinking and fanning fibers (Jbabdi and Johansen-Berg, 2011), while this is not possible for white matter BOLD-fMRI (Peer et al., 2017).

In addition, our work provided concurrent evidence that the profiles of white matter activity identified by tw-dFC are functionally meaningful. First, time profiles of white matter connectivity, similarly to what observed after dynamic connectivity analysis in the gray matter (Allen et al., 2014; Fan et al., 2021), show peculiar patterns of activity which are recurrent in time ("brain states"). The eleven white matter brain states identified in our work are in line with the corresponding gray matter brain states identified by hierarchical clustering of dynamic functional connectivity (Fan et al., 2021), by showing generally opposite patterns of activity between sensorimotor (visual, auditory, and somatomotor) white matter components (e.g. in states 5, 6, 9 and 11) and associative (default mode, frontoparietal, prefrontal and cerebellar) components (as in states 1, 2, 3, 7 or 10). These distinct sets of states are in line with the notion of "metastates", which involve preferentially sensorimotor or associative connectivity patterns, and which has been suggested to represent the basis for hierarchical organization of brain functional activity over time (Vidaurre et al., 2017). Further investigation of the temporal structure (e.g., transition probability or fractional time occupancy) of these brain states, could give interesting clues about their relation to inter-individual differences in brain function.

Second, correlation between time series components, as measured by FNC, revealed that dynamic activity in the white matter is coordinated across functionally homogeneous clusters, reflecting similarities in information processing. In the low-level representation of tw-dFC organization derived by ICA_{10}, FNC revealed a tripartite segregation into visual unimodal, somatosensory-auditory unimodal and associative transmodal brain regions. Along with reflecting the temporal activity patterns revealed by "brain states" hierarchical clustering, such a segregation is in line with the hierarchical organization model theorized previously by Mesulam (Mesulam, 1998) and recently confirmed by diffusion embedding of functional connectivity (Margulies et al., 2016). Moreover, this hierarchical organization is maintained also for increasingly fine-grained decompositions of the tw-dFC signal, where the tripartite model "breaks up" into multiple associative, sensorimotor, and visual clusters, each capturing distinct facets of cortico-cortical and cortico-subcortical information processing. In addition, while the cerebellar involvement is minimal in the ICA_{10}, and limited to a single component in the ICA_{20} (IC5, which covers cerebello-cerebellar connections via the middle cerebellar peduncle and is part of the "transmodal" cluster), FNC clustering of the higher-dimensionality ICA_{100} reveals distinct segregated cerebellar connectivity clusters, consisting of components covering intrinsic cerebellar connectivity or the cerebellar peduncles, either alone or in group with cerebral connectivity components. This result fits well with recent investigations postulating the existence of a hierarchical organization of cerebellum-cerebellar and cortical-cerebellar connectivity, similar to that observed for cerebral cortex (Guell et al., 2018).

Last but not least, FNC between time series components as derived by ICA_{100} can be successfully employed to predict behavior. This finding further confirms that the patterns of co-fluctuation between white matter components may be functionally relevant, by encoding inter-individual differences in behavioral traits. We choose to limit our analysis to higher-level cognition measures, which are frequently used in connectome-based prediction tasks (Finn et al., 2015) and, specifically, have been shown to be predictable by dynamic connectivity measures (Fan et al., 2021; Liu et al., 2018). Although we did not directly test the accuracy of predictions derived from tw-dFC data versus other static or dynamic connectivity methods, we suggest that tw-dFC-based behavioral prediction may show its usefulness by allowing a stronger link between functional measures and the underlying white matter anatomy, even considering that correlation between behavior and structural connectivity measures have been shown to be generally weaker than those obtained by functional connectivity (Lin et al., 2020; Miller et al., 2016; O'Muircheartaigh and Jbabdi, 2018). In the present work, mapping the spatial distribution of FNC-derived features predictive of cognitive performance allowed to identify functionally relevant structures, such as long and short-range white matter pathways involving the primary sensorimotor cortices, as well as frontoparietal and prefrontal bundles and connections involving the right cingulum, visual regions, and the cerebellum. In addition, our results reinforce the concept that complex cognitive activity may be not localized into single white matter units, but instead emerge from the coordinated activity of multiple independent white matter systems. However, it is worth to note that FNC measures as derived by ICA_{10} and ICA_{20} resulted in a few or no features surviving the features selection step and failed at providing statistically significant predictions and acceptable R^2 values. These findings may be due to the reduced FNC matrix dimensionality, which may be not sufficient to predict complex behavioral measures. In this scenario, further studies are warranted to probing the effect of different ICA dimensionalities on FNC-based cognitive performance prediction.

Taken together, these results confirm ICA-analysis of tw-dFC data as a powerful and versatile tool to investigate the relations between structural connectivity, functional activity, and behavior. Mapping behaviorally and clinically relevant functional information to the underlying white matter structures is of major relevance for a better understanding of brain functional anatomy in health and disease (Fox, 2018). Indeed, ICA analysis of tw-dFC data has potential translational application in diseases that involve direct damage to white matter bundles, such as stroke (Boes et al., 2015), traumatic brain injury (Hayes et al., 2016)or multiple sclerosis (Ravano et al., 2021). In addition, such a method may provide new insights into the pathophysiology of some neuropsychiatric conditions in which there is evidence of subtle white matter connectivity alterations such as epilepsy, schizophrenia, bipolar disorder, major depressive disorder or autism spectrum disorders (Koshiyama et al., 2020).

The present work does not come without limitations. The first concern regards the choice of dimensionality for the ICA decomposition of tw-dFC signal. In order to provide a compact representation of white matter independent components, we maintained our ICA dimensionality generally low, i.e., not more than 100 components, if compared to similar applications (O'Muircheartaigh and Jbabdi, 2018), and component stability was evaluated using ICASSO to avoid overfitting (Sai Ma et al., 2011). Another possible limitation is related to which dimension to impose maximized independence during ICA processing. Our choice towards spatial ICA (i.e., maximizing the independence of components in space instead of time) was substantially aimed at keeping our work consistent with most of the existing literature on ICA analysis of static and dynamic fMRI data (Damaraju et al., 2014; Fan et al., 2021; Smith et al., 2009). In addition, the choice of minimizing between-component correlation in space has permitted the conservation of higher degrees of correlation between component time series, which, as suggested by our findings, may encode biologically relevant information. However, imposing the constraint of spatial independence to white matter components could lead to oversimplification as multiple fiber populations, each with potentially different temporal profiles, may share the same spatial localization. Additional investigation using temporal ICA of tw-dFC data could add further insights on the temporal organization of white matter activity.

In addition, it is important to remark the role of non-neuronal sources (such as CSF pulsations, motion-related noise or cerebrovascular reactivity) as a potential confound when investigating dynamic fluctuations in functional connectivity (Preti et al., 2017). Although our results were obtained from nuisance-corrected fMRI data, preprocessed independently using two state-of-art denoising algorithms (Parkes et al., 2018), disentangling neuronal from non-neuronal signal in dynamic connectivity may be challenging even with the existing tools. On the other hand, constraining the dynamic functional connectivity analysis to voxels which are structurally connected by streamlines, as in tw-dFC, could help mitigate such drawback (Calamante et al., 2017). Nevertheless, it is generally well-known that tractography-derived priors may not entirely reflect the ground-truth white matter anatomy, being affected by relatively high false positive rates (Jbabdi and Johansen-Berg, 2011).

In the present work we employed a probabilistic tractography algorithm paired with track-filtering in the main dataset (multi-shell data), and the same algorithm without track-filtering in the validation dataset (single shell data). Albeit finding generally good external reproducibility, it remains difficult to rule out how much of the differences observed between the two datasets were due to tractography. Optimizing the tw-dFC map generation by integrating a tractography pipeline with high robustness to noise could help raising the external reproducibility of the resulting tw-dFC components, and the impact of different signal modeling. Finally, since the quality of tw-dFC maps depends on the correct alignment of tractography and BOLD-fMRI data, non-linear registration of tractograms, as well as proper distortion correction of both DWI and BOLD data, are critical steps that need accurate control to ensure the good quality of the results.

5. Conclusions

In the present work, we demonstrated that ICA decomposition of tw-dFC data may reliably identify spatial patterns of white matter connectivity, each showing distinct temporal profiles of activity. These spatial patterns, at the coarse scale, show similarity to well-known functional networks, and at increasing dimensionality are able to capture subtle anatomical details of white matter organization. Temporal patterns of activity in the white matter showed evidence of hierarchical organization at different levels, and their pattern of correlation may encode differences in behavioral traits.

In summary, we showed that tw-dFC is a powerful and versatile tool to investigate the relationships between brain structure, function, and behavior and it shows promise as a tool to deepen our knowledge on brain connectivity in health and disease.

Declaration of interest

The authors have nothing to declare.

Credit authorship contribution statement

Gianpaolo Antonio Basile: Conceptualization, Investigation, Writing – original draft, Writing – review & editing, Visualization. **Salvatore Bertino:** Conceptualization, Investigation, Writing – original draft, Writing – review & editing, Visualization. **Victor Nozais:** Writing – original draft, Writing – review & editing. **Alessia Bramanti:** Resources, Data curation. **Rosella Ciurleo:** Resources, Data curation. **Giuseppe Pio Anastasi:** Resources, Data curation, Writing – review & editing. **Demetrio Milardi:** Resources, Data curation, Writing – review & editing. **Alberto Cacciola:** Conceptualization, Investigation, Project administration, Supervision, Writing – original draft, Writing – review & editing.

Acknowledgments

The primary dataset (HCP) was provided by the Human Connectome Project, WU-Minn Consortium (Principal Investigators: David Van Essen and Kamil Ugurbil; 1U54MH091657), funded by the 16 NIH institutes and centers that support the NIH Blueprint for Neuroscience Research; and by the McDonnell Center for Systems Neuroscience at Washington University.

We also gratefully acknowledge the Mind-Body-Emotion group at the Max Planck Institute for Human Cognitive and Brain Sciences for the data of the “Leipzig Study for Mind-Body-Emotion Interactions” (LEMON) that have been used as validation dataset.

Data availability

The primary dataset (HCP) was provided by the Human Connectome Project, WU-Minn Consortium (Principal Investigators: David Van Essen and Kamil Ugurbil; 1U54MH091657), funded by the 16 NIH institutes and centers that support the NIH Blueprint for Neuroscience Research; and by the McDonnell Center for Systems Neuroscience at Washington University.

The “Leipzig Study for Mind-Body-Emotion Interactions” (LEMON) data that have been used as validation dataset was provided by the Mind-Body-Emotion group at the Max Planck Institute for Human Cognitive and Brain Sciences.

Funding information

This research was funded by the Italian Ministry of Health, Current Research Funds 2022.

The primary dataset (HCP) was provided by the Human Connectome Project, WU-Minn Consortium (Principal Investigators: David Van Essen and Kamil Ugurbil; 1U54MH091657), funded by the 16 NIH institutes and centers that support the NIH Blueprint for Neuroscience Research; and by the McDonnell Center for Systems Neuroscience at Washington University.

The “Leipzig Study for Mind-Body-Emotion Interactions” (LEMON) data that have been used as validation dataset was provided by the Mind-Body-Emotion group at the Max Planck Institute for Human Cognitive and Brain Sciences.

Supplementary materials

Supplementary material associated with this article can be found, in the online version, at doi:10.1016/j.neuroimage.2022.119391.

References

Allen, E.A., Damaraju, E., Plis, S.M., Erhardt, E.B., Eichele, T., Calhoun, V.D., 2014. Tracking whole-brain connectivity dynamics in the resting state. Cereb. Cortex 24, 663–676. doi:10.1093/CERCOR/BHS352.

Alves, P.N., Foulon, C., Karolis, V., Bzdok, D., Margulies, D.S., Volle, E., Thiebaut de Schotten, M., 2019. An improved neuroanatomical model of the default-mode network reconciles previous neuroimaging and neuropathological findings. Commun. Biol. 2, 370. doi:10.1038/s42003-019-0611-3.

Babayan, A., Erbey, M., Kumral, D., Reinelt, J.D., Reiter, A.M.F., Röbbig, J., Schaare, H.L., Uhlig, M., Anwander, A., Bazin, P.-L., Horstmann, A., Lampe, L., Nikulin, V.V., Okon-Singer, H., Preusser, S., Pampel, A., Rohr, C.S., Sacher, J., Thöne-Otto, A., Trapp, S., Nierhaus, T., Altmann, D., Arelin, K., Blöchl, M., Bongartz, E., Breig, P., Cesnaite, E., Chen, S., Cozatl, R., Czerwonatis, S., Dambrauskaite, G., Dreyer, M., Enders, J., Engelhardt, M., Fischer, M.M., Forschack, N., Golchert, J., Golz, L., Guran, C.A., Hedrich, S., Hentschel, N., Hoffmann, D.I., Huntenburg, J.M., Jost, R., Kosatschek, A., Kunzendorf, S., Lammers, H., Lauckner, M.E., Mahjoory, K., Kanaan, A.S., Mendes, N., Menger, R., Morino, E., Näthe, K., Neubauer, J., Noyan, H., Oligschläger, S., Panczyszyn-Trzewik, P., Poehlchen, D., Putzke, N., Roski, S., Schaller, M.-C., Schieferbein, A., Schlaak, B., Schmidt, R., Gorgolewski, K.J., Schmidt, H.M., Schrimpf, A., Stasch, S., Voss, M., Wiedemann, A., Margulies, D.S., Gaebler, M., Villringer, A., 2019. A mind-brain-body dataset of MRI, EEG, cognition, emotion, and peripheral physiology in young and old adults. Sci. Data 6, 180308. doi:10.1038/sdata.2018.308.

Barbeau, E.B., Descoteaux, M., Petrides, M., 2020. Dissociating the white matter tracts connecting the temporo-parietal cortical region with frontal cortex using diffusion tractography. Sci. Rep. 10, 1–13. doi:10.1038/s41598-020-64124-y.

Basile, G.A., Bertino, S., Bramanti, A., Anastasi, G.P., Milardi, D., Cacciola, A., 2021. In Vivo Super-Resolution Track-Density Imaging for Thalamic Nuclei Identification. Cereb. Cortex. doi:10.1093/cercor/bhab184.

Basile, G.A., Bramanti, A., Bertino, S., Cutroneo, G., Bruno, A., Tisano, A., Paladina, G., Milardi, D., Anastasi, G., 2020. Structural connectivity-based parcellation of the dopaminergic midbrain in healthy subjects and schizophrenic patients. Medicina (Kaunas) 56, 1–13. doi:10.3390/medicina56120686.

Bell, A.J., Sejnowski, T.J., 1995. An Information-Maximization Approach to Blind Separation and Blind Deconvolution. Neural Comput 7, 1129–1159. doi:10.1162/neco.1995.7.6.1129.

Bertino, S., Basile, G.A., Anastasi, G., Bramanti, A., Fonti, B., Cavallaro, F., Bruschetta, D., Milardi, D., Cacciola, A., 2020a. Anatomical characterization of the human structural connectivity between the pedunculopontine nucleus and globus pallidus via multi-shell multi-tissue tractography. Medicina (Kaunas) 56. doi:10.3390/medicina56090452, E452.

Bertino, S., Basile, G.A., Bramanti, A., Anastasi, G.P., Quartarone, A., Milardi, D., Cacciola, A., 2020b. Spatially coherent and topographically organized pathways of the human globus pallidus. Hum. Brain Mapp. 1–21. doi:10.1002/hbm.25147.

Bertino, S., Basile, G.A., Bramanti, A., Ciurleo, R., Tisano, A., Anastasi, G.P., Milardi, D., Cacciola, A., 2021. Ventral intermediate nucleus structural connectivity-derived segmentation: anatomical reliability and variability. Neuroimage 243, 118519. doi:10.1016/j.neuroimage.2021.118519.

Boes, A.D., Prasad, S., Liu, H., Liu, Q., Pascual-Leone, A., Caviness, V.S., Fox, M.D., 2015. Network localization of neurological symptoms from focal brain lesions. Brain 138, 3061–3075. doi:10.1093/brain/awv228.

Buckner, R.L., Sepulcre, J., Talukdar, T., Krienen, F.M., Liu, H., Hedden, T., Andrews-Hanna, J.R., Sperling, R.A., Johnson, K.A., 2009. Cortical Hubs Revealed by Intrinsic Functional Connectivity: Mapping, Assessment of Stability, and Relation to Alzheimer's Disease. J. Neurosci. 29, 1860. doi:10.1523/JNEUROSCI.5062-08.2009.

Cacciola, A., Bertino, S., Basile, G.A., Di Mauro, D., Calamuneri, A., Chillemi, G., Duca, A., Bruschetta, D., Flace, P., Favaloro, A., Calabrò, R.S., Anastasi, G., Milardi, D., 2019. Mapping the structural connectivity between the periaqueductal gray and the cerebellum in humans. Brain Struct. Funct. doi:10.1007/s00429-019-01893-x.

Cacciola, A., Milardi, D., Anastasi, G.P., Basile, G.A., Ciolli, P., Irrera, M., Cutroneo, G., Bruschetta, D., Rizzo, G., Mondello, S., Bramanti, P., Quartarone, A., 2016. A Direct Cortico-Nigral Pathway as Revealed by Constrained Spherical Deconvolution Tractography in Humans. Front. Hum. Neurosci. 10, 374. doi:10.3389/fnhum.2016.00374.

Calamante, F., 2017. Track-weighted imaging methods: extracting information from a streamlines tractogram. Magn. Reson. Mater. Physics, Biol. Med. doi:10.1007/s10334-017-0608-1.

Calamante, F., Smith, R.E., Liang, X., Zalesky, A., Connelly, A., 2017. Track-weighted dynamic functional connectivity (TW-dFC): a new method to study time-resolved functional connectivity. Brain Struct. Funct. 222, 3761–3774. doi:10.1007/s00429-017-1431-1.

Calamante, F., Tournier, J.D., Smith, R.E., Connelly, A., 2012. A generalised framework for super-resolution track-weighted imaging. Neuroimage doi:10.1016/j.neuroimage.2011.08.099.

Calhoun, V.D., Adali, T., Pearlson, G.D., Pekar, J.J., 2001. A method for making group inferences from functional MRI data using independent component analysis. Hum. Brain Mapp doi:10.1002/hbm.1048.

Damaraju, E., Allen, E.A., Belger, A., Ford, J.M., McEwen, S., Mathalon, D.H., Mueller, B.A., Pearlson, G.D., Potkin, S.G., Preda, A., Turner, J.A., Vaidya, J.G., van Erp, T.G., Calhoun, V.D., 2014. Dynamic functional connectivity analysis reveals transient states of dysconnectivity in schizophrenia. NeuroImage Clin 5, 298–308. doi:10.1016/j.nicl.2014.07.003.

Damoiseaux, J.S., Rombouts, S.A.R.B., Barkhof, F., Scheltens, P., Stam, C.J., Smith, S.M., Beckmann, C.F., 2006. Consistent resting-state networks across healthy subjects. Proc. Natl. Acad. Sci. 103, 13848–13853. https://doi.org/10.1073/pnas.0601417103

Dhollander, T., Raffelt, D., Connelly, A., 2016. Unsupervised 3-tissue response function estimation from single-shell or multi-shell diffusion MR data without a co-registered T1 image. In: ISMRM Workshop on Breaking the Barriers of Diffusion MRI, p. 5.

Di, X., Gohel, S., Kim, E.H., Biswal, B.B., 2013. Task vs. rest—different network configurations between the coactivation and the resting-state brain networks. Front. Hum. Neurosci. 7. doi:10.3389/fnhum.2013.00493.

Dice, L.R., 1945. Measures of the Amount of Ecologic Association Between Species. Ecology doi:10.2307/1932409.

Draganski, B., Kherif, F., Klöppel, S., Cook, P.A., Alexander, D.C., Parker, G.J.M., Deichmann, R., Ashburner, J., Frackowiak, R.S.J., Kloppel, S., Cook, P.A., Alexander, D.C., Parker, G.J.M., Deichmann, R., Ashburner, J., Frackowiak, R.S.J., 2008. Evidence for Segregated and Integrative Connectivity Patterns in the Human Basal Ganglia. J. Neurosci. 28, 7143–7152. doi:10.1523/JNEUROSCI.1486-08.2008.

Du, Y., Fan, Y., 2013. Group information guided ICA for fMRI data analysis. Neuroimage 69, 157–197. doi:10.1016/j.neuroimage.2012.11.008.

Fox, M.D., 2018. Mapping symptoms to brain networks with the human connectome. N. Eng. J. Med. 379, 2237–2245. doi:10.1056/NEJMra1706158.

Eickhoff, S.B., Bzdok, D., Laird, A.R., Roski, C., Caspers, S., Zilles, K., Fox, P.T., 2011. Co-activation patterns distinguish cortical modules, their connectivity and functional differentiation. Neuroimage 57, 938–949. doi:10.1016/j.neuroimage.2011.05.021.

Erhardt, E.B., Rachakonda, S., Bedrick, E.J., Allen, E.A., Adali, T., Calhoun, V.D., 2011. Comparison of multi-subject ICA methods for analysis of fMRI data. Hum. Brain Mapp. 32, 2075–2095. doi:10.1002/hbm.21170.

Fan, L., Zhong, Q., Qin, J., Li, N., Su, J., Zeng, L.-L., Hu, D., Shen, H., 2021. Brain parcellation driven by dynamic functional connectivity better capture intrinsic network dynamics. Hum. Brain Mapp. 42, 1416–1433. doi:10.1002/HBM.25303.

Figley, T.D., Mortazavi Moghadam, B., Bhullar, N., Kornelsen, J., Courtney, S.M., Figley, C.R., 2017. Probabilistic White Matter Atlases of Human Auditory, Basal Ganglia, Language, Precuneus, Sensorimotor, Visual and Visuospatial Networks. Front. Hum. Neurosci. 11. doi:10.3389/fnhum.2017.00306.

Finger, H., Bönstrup, M., Cheng, B., Messé, A., Hilgetag, C., Thomalla, G., Gerloff, C., König, P., 2016. Modeling of Large-Scale Functional Brain Networks Based on Structural Connectivity from DTI: Comparison with EEG Derived Phase Coupling Networks and Evaluation of Alternative Methods along the Modeling Path. PLOS Comput. Biol. 12, e1005025. doi:10.1371/journal.pcbi.1005025.

Finn, E.S., Shen, X., Scheinost, D., Rosenberg, M.D., Huang, J., Chun, M.M., Papademetris, X., Constable, R.T., 2015. Functional connectome fingerprinting: Identifying individuals using patterns of brain connectivity. Nat. Neurosci. doi:10.1038/nn.4135.

Friedrich, P., Forkel, S.J., Thiebaut de Schotten, M., 2020. Mapping the principal gradient onto the corpus callosum. Neuroimage 223, 117317. doi:10.1016/j.neuroimage.2020.117317.

Gawryluk, J.R., Mazerolle, E.L., D'Arcy, R.C.N., 2014. Does functional MRI detect activation in white matter? A review of emerging evidence, issues, and future directions. Front. Neurosci. 8. doi:10.3389/fnins.2014.00239.

Glasser, M.F., Sotiropoulos, S.N., Wilson, J.A., Coalson, T.S., Fischl, B., Andersson, J.L., Xu, J., Jbabdi, S., Webster, M., Polimeni, J.R., Van Essen, D.C., Jenkinson, M., 2013. The minimal preprocessing pipelines for the Human Connectome Project. Neuroimage 80, 105–124. doi:10.1016/j.neuroimage.2013.04.127.

Griffa, A., Ricaud, B., Benzi, K., Bresson, X., Daducci, A., Vandergheynst, P., Thiran, J.P., Hagmann, P., 2017. Transient networks of spatio-temporal connectivity map communication pathways in brain functional systems. Neuroimage 155, 490–502. doi:10.1016/J.NEUROIMAGE.2017.04.015.

Guell, X., Schmahmann, J.D., Gabrieli, J.D.E., Ghosh, S.S., 2018. Functional gradients of the cerebellum. Elife 7, 1–22. doi:10.7554/eLife.36652.

Gutiérrez-Gómez, L., Vohryzek, J., Chiêm, B., Baumann, P.S., Conus, P., Cuenod, K.Do, Hagmann, P., Delvenne, J.C., 2020. Stable biomarker identification for predicting schizophrenia in the human connectome. NeuroImage Clin 27, 102316. doi:10.1016/J.NICL.2020.102316.

Hayes, J.P., Bigler, E.D., Verfaellie, M., 2016. Traumatic Brain Injury as a Disorder of Brain Connectivity. J. Int. Neuropsychol. Soc. 22, 120–137. doi:10.1017/S1355617715000740.

Honey, C.J., Sporns, O., Cammoun, L., Gigandet, X., Thiran, J.P., Meuli, R., Hagmann, P., 2009. Predicting human resting-state functional connectivity from structural connectivity. Proc. Natl. Acad. Sci. 106, 2035–2040. https://doi.org/10.1073/pnas.0811168106

Horn, A., Ostwald, D., Reisert, M., Blankenburg, F., 2014. The structural–functional connectome and the default mode network of the human brain. Neuroimage 102, 142–151. doi:10.1016/j.neuroimage.2013.09.069.

Hua, K., Zhang, J., Wakana, S., Jiang, H., Li, X., Reich, D.S., Calabresi, P.A., Pekar, J.J., van Zijl, P.C.M., Mori, S., 2008. Tract probability maps in stereotaxic spaces: Analyses of white matter anatomy and tract-specific quantification. Neuroimage 39, 336–347. doi:10.1016/j.neuroimage.2007.07.053.

Huang, Y., Yang, Y., Hao, L., Hu, X., Wang, P., Ding, Z., Gao, J.-H., Gore, J.C., 2020. Detection of functional networks within white matter using independent component analysis. Neuroimage 222, 117278. doi:10.1016/j.neuroimage.2020.117278.

Jbabdi, S., Johansen-Berg, H., 2011. Tractography: Where Do We Go from Here? Brain Connect 1, 169–183. doi:10.1089/brain.2011.0033.

Jeurissen, B., Tournier, J.D., Dhollander, T., Connelly, A., Sijbers, J., 2014. Multi-tissue constrained spherical deconvolution for improved analysis of multi-shell diffusion MRI data. Neuroimage 103, 411–426. doi:10.1016/j.neuroimage.2014.07.061.

Koshiyama, D., Fukunaga, M., Okada, N., Morita, K., Nemoto, K., Usui, K., Yamamori, H., Yasuda, Y., Fujimoto, M., Kudo, N., Azechi, H., Watanabe, Y., Hashimoto, N., Narita, H., Kusumi, I., Ohi, K., Shimada, T., Kataoka, Y., Yamamoto, M., Ozaki, N., Okada, G., Okamoto, Y., Harada, K., Matsuo, K., Yamasue, H., Abe, O., Hashimoto, Ryuichiro, Takahashi, T., Hori, T., Nakataki, M., Onitsuka, T., Holleran, L., Jahanshad, N., van Erp, T.G.M., Turner, J., Donohoe, G., Thompson, P.M., Kasai, K., Hashimoto, Ryota, 2020. White matter microstructural alterations across four major psychiatric disorders: mega-analysis study in 2937 individuals. Mol. Psychiatry 25, 883–895. doi:10.1038/s41380-019-0553-7.

Leonardi, N., Van De Ville, D., 2015. On spurious and real fluctuations of dynamic functional connectivity during rest. Neuroimage 104, 430–436. doi:10.1016/j.neuroimage.2014.09.007.

Lin, Y., Baete, S.H., Wang, X., Boada, F.E., 2020. Mapping brain–behavior networks using functional and structural connectome fingerprinting in the HCP dataset. Brain Behav 10. doi:10.1002/brb3.1647.

Liu, J., Liao, X., Xia, M., He, Y., 2018. Chronnectome fingerprinting: Identifying individuals and predicting higher cognitive functions using dynamic brain connectivity patterns. Hum. Brain Mapp. 39, 902–915. doi:10.1002/HBM.23890.

Margulies, D.S., Ghosh, S.S., Goulas, A., Falkiewicz, M., Huntenburg, J.M., Langs, G., Bezgin, G., Eickhoff, S.B., Castellanos, F.X., Petrides, M., Jefferies, E., Smallwood, J., 2016. Situating the default-mode network along a principal gradient of macroscale cortical organization. Proc. Natl. Acad. Sci. U. S. A. doi:10.1073/pnas.1608282113.

Mesulam, M., 1998. From sensation to cognition. Brain 121, 1013–1052. doi:10.1093/brain/121.6.1013.

Milardi, D., Basile, G.A., Faskowitz, J., Bertino, S., Quartarone, A., Anastasi, G.P., Bramanti, A., Ciurleo, R., Cacciola, A., 2022. Effects of diffusion signal modeling and segmentation approaches on subthalamic nucleus parcellation. Neuroimage 250, 118959. doi:10.1016/j.neuroimage.2022.118959.

Milardi, D., Quartarone, A., Bramanti, A., Anastasi, G., Bertino, S., Basile, G.A., Buonasera, P., Pilone, G., Celeste, G., Rizzo, G., Bruschetta, D., Cacciola, A., 2019. The Cortico-Basal Ganglia-Cerebellar Network: Past, Present and Future Perspectives. Front. Syst. Neurosci. 61. doi:10.3389/fnsys.2019.00061.

Miller, K.L., Alfaro-Almagro, F., Bangerter, N.K., Thomas, D.L., Yacoub, E., Xu, J., Bartsch, A.J., Jbabdi, S., Sotiropoulos, S.N., Andersson, J.L.R., Griffanti, L., Douaud, G., Okell, T.W., Weale, P., Dragonu, I., Garratt, S., Hudson, S., Collins, R., Jenkinson, M., Matthews, P.M., Smith, S.M., 2016. Multimodal population brain imaging in the UK Biobank prospective epidemiological study. Nat. Neurosci. 19, 1523–1536. doi:10.1038/nn.4393.

Nichols, T.E., Das, S., Eickhoff, S.B., Evans, A.C., Glatard, T., Hanke, M., Kriegeskorte, N., Milham, M.P., Poldrack, R.A., Poline, J.-B., Proal, E., Thirion, B., Van Essen, D.C., White, T., Yeo, B.T.T., 2017. Best practices in data analysis and sharing in neuroimaging using MRI. Nat. Neurosci. 20, 299–303. doi:10.1038/nn.4500.

Nozais, V., Forkel, S.J., Foulon, C., Petit, L., Thiebaut de Schotten, M., 2021. Functionnectome as a framework to analyse the contribution of brain circuits to fMRI. Commun. Biol. 4, 1035. doi:10.1038/s42003-021-02530-2.

O'Muircheartaigh, J., Jbabdi, S., 2018. Concurrent white matter bundles and grey matter networks using independent component analysis. Neuroimage 170, 296–306. doi:10.1016/j.neuroimage.2017.05.012.

Parkes, L., Fulcher, B., Yücel, M., Fornito, A., 2018. An evaluation of the efficacy, reliability, and sensitivity of motion correction strategies for resting-state functional MRI. Neuroimage 171, 415–436. doi:10.1016/j.neuroimage.2017.12.073.

Peer, M., Nitzan, M., Bick, A.S., Levin, N., Arzy, S., 2017. Evidence for Functional Networks within the Human Brain's White Matter. J. Neurosci. 37, 6394–6407. doi:10.1523/JNEUROSCI.3872-16.2017.

Plachti, A., Eickhoff, S.B., Hoffstaedter, F., Patil, K.R., Laird, A.R., Fox, P.T., Amunts, K., Genon, S., 2019. Multimodal Parcellations and Extensive Behavioral Profiling Tackling the Hippocampus Gradient. Cereb. Cortex 29, 4595–4612. doi:10.1093/cercor/bhy336.

Preti, M.G., Bolton, T.A., Van De Ville, D., 2017. The dynamic functional connectome: State-of-the-art and perspectives. Neuroimage 160, 41–54. doi:10.1016/J.NEUROIMAGE.2016.12.061.

Qin, J., Chen, S., Hu, D., Zeng, L., Fan, Y., Chen, X., Shen, H., 2015. Predicting individual brain maturity using dynamic functional connectivity. Front. Hum. Neurosci. 9. doi:10.3389/FNHUM.2015.00418.

Raichle, M.E., 2015. The restless brain: How intrinsic activity organizes brain function. Philos. Trans. R. Soc. B Biol. Sci. 370. doi:10.1098/RSTB.2014.0172.

Ravano, V., Andelova, M., Fartaria, M.J., Mahdi, M.F.A.-W., Maréchal, B., Meuli, R., Uher, T., Krasensky, J., Vaneckova, M., Horakova, D., Kober, T., Richiardi, J., 2021. Validating atlas-based lesion disconnectomics in multiple sclerosis: A retrospective multi-centric study. NeuroImage Clin 32, 102817. doi:10.1016/j.nicl.2021.102817.

Rolls, E.T., Huang, C.-C., Lin, C.-P., Feng, J., Joliot, M., 2020. Automated anatomical labelling atlas 3. Neuroimage 206, 116189. https://doi.org/10.1016/j.neuroimage.2019.116189

Ma, Sai, Correa, N.M., Li, Xi-Lin, Eichele, T., Calhoun, V.D., Adali, T., 2011. Automatic Identification of Functional Clusters in fMRI Data Using Spatial Dependence. IEEE Trans. Biomed. Eng. 58, 3406–3417. doi:10.1109/TBME.2011.2167149.

Salimi-Khorshidi, G., Douaud, G., Beckmann, C.F., Glasser, M.F., Griffanti, L., Smith, S.M., 2014. Automatic denoising of functional MRI data: Combining independent component analysis and hierarchical fusion of classifiers. Neuroimage 90, 449–468. doi:10.1016/j.neuroimage.2013.11.046.

Sanchez, E., El-Khatib, H., Arbour, C., Bedetti, C., Blais, H., Marcotte, K., Baril, A.-A., Descoteaux, M., Gilbert, D., Carrier, J., Gosselin, N., 2019. Brain white matter damage and its association with neuronal synchrony during sleep. Brain 142, 674–687. doi:10.1093/brain/awy348.

Shrout, P.E., Fleiss, J.L., 1979. Intraclass correlations: Uses in assessing rater reliability. Psychol. Bull. 86, 420–428. doi:10.1037/0033-2909.86.2.420.

Smith, A.J., Blumenfeld, H., Behar, K.L., Rothman, D.L., Shulman, R.G., Hyder, F., 2002. Cerebral energetics and spiking frequency: The neurophysiological basis of fMRI. Proc. Natl. Acad. Sci. 99, 10765–10770. https://doi.org/10.1073/pnas.132272199

Smith, R.E., Tournier, J.D., Calamante, F., Connelly, A., 2015. The effects of SIFT on the reproducibility and biological accuracy of the structural connectome. Neuroimage 104, 253–265. doi:10.1016/j.neuroimage.2014.10.004.

Smith, R.E., Tournier, J.D., Calamante, F., Connelly, A., 2012. Anatomically-constrained tractography: Improved diffusion MRI streamlines tractography through effective use of anatomical information. Neuroimage 62, 1924–1938. doi:10.1016/j.neuroimage.2012.06.005.

Smith, S., Fox, PT, Miller, K., Glahn, D., Fox, PM, Mackay, C., Filippini, N., Watkins, K., Toro, L., Laird, A., Beckmann, C., 2009. Correspondence of the brain's functional architecture during activation and rest. Proc. Natl. Acad. Sci. U. S. A. 106, 13040–13045. doi:10.1073/PNAS.0905267106.

Smith, S.M., Beckmann, C.F., Andersson, J., Auerbach, E.J., Bijsterbosch, J., Douaud, G., Duff, E., Feinberg, D.A., Griffanti, L., Harms, M.P., Kelly, M., Laumann, T., Miller, K.L., Moeller, S., Petersen, S., Power, J., Salimi-Khorshidi, G., Snyder, A.Z., Vu, A.T., Woolrich, M.W., Xu, J., Yacoub, E., Uğurbil, K., Van Essen, D.C., Glasser, M.F., 2013. Resting-state fMRI in the Human Connectome Project. Neuroimage 80, 144–168. doi:10.1016/j.neuroimage.2013.05.039.

Stoodley, C.J., Schmahmann, J.D., 2018. Functional topography of the human cerebellum. Handbook of Clinical Neurology 59–70. doi:10.1016/B978-0-444-63956-1.00004-7.

Tavor, I., Jones, O.P., Mars, R.B., Smith, S.M., Behrens, T.E., Jbabdi, S., 2016. Task-free MRI predicts individual differences in brain activity during task performance. Science 352, 216–220. doi:10.1126/science.aad8127, 80-.

Tournier, J.D., Calamante, F., Connelly, A., 2010. Improved probabilistic streamlines tractography by 2nd order integration over fibre orientation distributions. Proc. Int. Soc. Magn. Reson. Med..

Tournier, J.D., Smith, R., Raffelt, D., Tabbara, R., Dhollander, T., Pietsch, M., Christiaens, D., Jeurissen, B., Yeh, C.H., Connelly, A., 2019. MRtrix3: A fast, flexible and open software framework for medical image processing and visualisation. Neuroimage doi:10.1016/j.neuroimage.2019.116137.

Tournier, J.D., Yeh, C.H., Calamante, F., Cho, K.H., Connelly, A., Lin, C.P., 2008. Resolving crossing fibres using constrained spherical deconvolution: Validation using diffusion-weighted imaging phantom data. Neuroimage 42, 617–625. doi:10.1016/j.neuroimage.2008.05.002.

Tustison, N.J., Avants, B.B., Cook, P.A., Zheng, Y., Egan, A., Yushkevich, P.A., Gee, J.C., 2010. N4ITK: improved N3 bias correction. IEEE Trans. Med. Imaging 29, 1310–1320. doi:10.1109/TMI.2010.2046908.

Uğurbil, K., Xu, J., Auerbach, E.J., Moeller, S., Vu, A.T., Duarte-Carvajalino, J.M., Lenglet, C., Wu, X., Schmitter, S., Van de Moortele, P.F., Strupp, J., Sapiro, G., De Martino, F., Wang, D., Harel, N., Garwood, M., Chen, L., Feinberg, D.A., Smith, S.M., Miller, K.L., Sotiropoulos, S.N., Jbabdi, S., Andersson, J.L.R., Behrens, T.E.J., Glasser, M.F., Van Essen, D.C., Yacoub, E., 2013. Pushing spatial and temporal resolution for functional and diffusion MRI in the Human Connectome Project. Neuroimage 80, 80–104. doi:10.1016/j.neuroimage.2013.05.012.

van den Heuvel, M.P., Stam, C.J., Kahn, R.S., Hulshoff Pol, H.E., 2009. Efficiency of functional brain networks and intellectual performance. J. Neurosci. 29, 7619–7624. doi:10.1523/JNEUROSCI.1443-09.2009.

Van Essen, D.C., Smith, S.M., Barch, D.M., Behrens, T.E.J., Yacoub, E., Ugurbil, K., 2013. The WU-Minn Human Connectome Project: An overview. Neuroimage 80, 62–79. doi:10.1016/j.neuroimage.2013.05.041.

Vidaurre, D., Smith, S.M., Woolrich, M.W., 2017. Brain network dynamics are hierarchically organized in time. Proc. Natl. Acad. Sci. 114, 12827–12832. https://doi.org/10.1073/pnas.1705120114

Ward, J.H., 1963. Hierarchical Grouping to Optimize an Objective Function. J. Am. Stat. Assoc. 58, 236–244. doi:10.1080/01621459.1963.10500845.

Whitfield-Gabrieli, S., Nieto-Castanon, A., 2012. *Conn* : A Functional Connectivity Toolbox for Correlated and Anticorrelated Brain Networks. Brain Connect 2, 125–141. doi:10.1089/brain.2012.0073.

Wu, L., Calhoun, V.D., Jung, R.E., Caprihan, A., 2015. Connectivity-based whole brain dual parcellation by group ICA reveals tract structures and decreased connectivity in schizophrenia. Hum. Brain Mapp 36, 4681–4701. doi:10.1002/hbm.22945.

Xing, X.X., Zuo, X.N., 2018. The anatomy of reliability: a must read for future human brain mapping. Sci. Bull. 63, 1606–1607. doi:10.1016/j.scib.2018.12.010.

Yeh, F.-C., Panesar, S., Fernandes, D., Meola, A., Yoshino, M., Fernandez-Miranda, J.C., Vettel, J.M., Verstynen, T., 2018. Population-averaged atlas of the macroscale human structural connectome and its network topology. Neuroimage 178, 57–68. doi:10.1016/j.neuroimage.2018.05.027.

Zuo, X.N., Biswal, B.B., Poldrack, R.A., 2019. Editorial: Reliability and reproducibility in functional connectomics. Front. Neurosci. 13, 1–4. doi:10.3389/fnins.2019.00117.